



Title	Analysis of the tropical tropopause layer using the Nonhydrostatic Icosahedral Atmospheric Model (NICAM) : 2. An experiment under the atmospheric conditions of December 2006 to January 2007
Author(s)	Kubokawa, H.; Fujiwara, M.; Nasuno, T.; Miura, M.; Yamamoto, M. K.; Satoh, M.
Citation	Journal of Geophysical Research: Atmospheres, 117(D17), D17114 https://doi.org/10.1029/2012JD017737
Issue Date	2012-09-11
Doc URL	http://hdl.handle.net/2115/64769
Rights	Copyright 2012 American Geophysical Union
Type	article
File Information	Kubokawa_et_al-2012-Journal_of_Geophysical_Research__Atmospheres_(1984-2012).pdf



[Instructions for use](#)

Analysis of the tropical tropopause layer using the Nonhydrostatic Icosahedral Atmospheric Model (NICAM):

2. An experiment under the atmospheric conditions of December 2006 to January 2007

H. Kubokawa,^{1,2} M. Fujiwara,¹ T. Nasuno,³ M. Miura,⁴ M. K. Yamamoto,⁵ and M. Satoh^{3,4}

Received 6 March 2012; revised 18 July 2012; accepted 18 July 2012; published 11 September 2012.

[1] The roles of deep convection and generated waves in the Tropical Tropopause Layer (TTL) are investigated using a global nonhydrostatic model, the Nonhydrostatic Icosahedral Atmospheric Model (NICAM), which runs on the Earth Simulator with a horizontal spacing of 7 km. The model data, which successfully simulated a Madden-Julian Oscillation (MJO) event for the period between 15 December 2006 and 15 January 2007, are analyzed. The frequency of deep convective clouds that reach the TTL is one of the key diagnostics for dehydration and transport. The present results revealed that the proportion of cumulus clouds that penetrate the lapse-rate tropopause and the bottom boundary of the TTL (defined as the lapse rate minimum) is $\sim 0.5\%$ and $\sim 20\%$, respectively, in the region between 5°S and 5°N . This result is reasonably consistent with atmospheric observations. Deep convective activity that reaches the TTL was observed over southern Africa, the Indian Ocean, the Indonesian maritime continent, the western Pacific, and southern America. Deep convection over the continents was most active during the local evening period. Over the oceans, high clouds reaching the tropopause were seen over the Indian Ocean and the seas around Java, where two tropical cyclones were generated. Prominent diurnal variations in tropopause temperature associated with deep convection occurred over the Indonesian maritime continent. These diurnal variations were superimposed on large, low-frequency temperature variations associated with equatorial Kelvin waves generated by the MJO convection. Probably because of coarse vertical resolution, temperature variations simulated by the NICAM are larger than those in the real atmosphere. The two tropical cyclones caused relatively large tropopause temperature variations with a cyclone scale (~ 500 km horizontally). The gravity waves generated by tropical cyclones cause small tropopause temperature variations that extend for 1000 km from the cyclone. We conclude that the Kelvin waves associated with the MJO convection cause the largest amplitude of temperature variations in the TTL and that tropical cyclones and diurnal variations of convective activity have large local impacts on temperature variations in the TTL.

Citation: Kubokawa, H., M. Fujiwara, T. Nasuno, M. Miura, M. K. Yamamoto, and M. Satoh (2012), Analysis of the tropical tropopause layer using the Nonhydrostatic Icosahedral Atmospheric Model (NICAM): 2. An experiment under the atmospheric conditions of December 2006 to January 2007, *J. Geophys. Res.*, *117*, D17114, doi:10.1029/2012JD017737.

1. Introduction

[2] The tropical tropopause layer (TTL) is a transition region between the troposphere and the stratosphere, and is the primary entrance region for tropospheric air passing

through to the stratosphere [e.g., Fueglistaler *et al.*, 2009]. Water vapor entering the stratosphere is controlled by the temperature field in this region. Tropical deep convection and various waves around the tropopause are the main

¹Graduate School of Environmental Science, Hokkaido University, Sapporo, Japan.

Corresponding author: H. Kubokawa, Atmosphere and Ocean Research Institute, University of Tokyo, 5-1-5, Kashiwanoha, Kashiwa, Chiba 277-8568, Japan. (kubok@aori.u-tokyo.ac.jp)

This paper is not subject to U.S. copyright. Published in 2012 by the American Geophysical Union.

²Now at Atmosphere and Ocean Research Institute, University of Tokyo, Kashiwa, Japan.

³Research Institute for Global Change, Japan Agency for Marine-Earth Science and Technology, Yokohama, Japan.

⁴Atmosphere and Ocean Research Institute, University of Tokyo, Kashiwa, Japan.

⁵Division of Diagnostics and Control of Humansphere, Research Divisions, Research Institute for Sustainable Humansphere, Kyoto University, Gokasho, Japan.

factors controlling this temperature field. However, it is difficult to observe in-cloud properties, and thus the role of deep convection in temperature variations is still not well understood. Deep convection also acts as an agent for the rapid transport of near-surface air into the TTL, and sometimes directly into the lower stratosphere. *Kley et al.* [1996] identify the important role of deep convection in the transport of ozone from the marine boundary layer to the tropopause, although *Vömel and Diaz* [2010] suggest that there is an error within the measurements of *Kley et al.* [1996]. It is also thought that tropical deep convective transport is particularly important for brominated Very-Short-Lived Substances (VSLS) that are emitted from the ocean, with higher emissions in tropical coastal regions [*World Meteorological Organization*, 2007, chapter 2], and that brominated VSLS make a significant contribution to total stratospheric bromine, and consequently to the stratospheric ozone budget. In contrast, continental emissions include hydrocarbons and volatile organic compounds, in addition to NO_x and CO near the surface [*Barth et al.*, 2007]. Consequently, tropical deep convection is an important factor in determining the concentration of photochemically active species in both the TTL and the stratosphere. *Liu and Zipser* [2005] and *Iwasaki et al.* [2010] show that cloud-top altitudes over the continents are generally higher than those over the oceans. However, neither considered the detailed local time dependence of deep convective activity in each region, which may be very important photochemically [e.g., *Barth et al.*, 2007].

[3] As discussed in our previous paper [*Kubokawa et al.*, 2010], many studies have investigated the role of deep convective clouds in the temperature field around the tropopause. Both mesoscale, and cloud-resolving models have been used to examine the role of deep convection in controlling dehydration within the TTL [*Potter and Holton*, 1995; *Chaboureaud et al.*, 2007; *Grosvenor et al.*, 2007], in the heat and mass budget of the TTL [*Kuang and Bretherton*, 2004; *Küpper et al.*, 2004], and in rapid transport of near-surface air into the TTL [*Barth et al.*, 2007]. However, such models are restricted to limited horizontal domains, and they inherently lack the interaction between small- to meso-scale disturbances and large-scale disturbances to the general circulation, which are essential in the tropics [e.g., *Madden and Julian*, 1994]. To address this problem, *Kubokawa et al.* [2010] analyzed data from the aqua planet experiments using a global nonhydrostatic model: the Nonhydrostatic Icosahedral Atmospheric Model (NICAM) [*Sato et al.*, 2008; *Tomita and Sato*, 2004], which runs on the Earth Simulator with a horizontal spacing of 3.5 and 7 km.

[4] In this paper, we analyze NICAM data generated under realistic atmospheric conditions for the period between December 2006 and January 2007. *Miura et al.* [2007] report that an MJO event is realistically simulated in this model simulations, reproducing the multiscale structure of tropical convection [e.g., *Masunaga et al.*, 2008; *Nasuno et al.*, 2009; *Liu et al.*, 2009]. Thus, this experiment is referred to as a NICAM MJO experiment. *Fudeyasu et al.* [2008, 2010a, 2010b] report that two observed tropical cyclones, Bond (which first appeared on 18 December 2006) and Isobel (which first appeared on 29 December 2006) over the Indian Ocean, are also realistically simulated in this model simulations. *Sato et al.* [2009] show that the diurnal cycles of precipitation in the tropics are also reasonably well

simulated. We will therefore investigate the roles of these cloud disturbances on temperature variability in the TTL. Compared with the aqua planet experiment analyzed by *Kubokawa et al.* [2010], the MJO experiment include a realistic orography and sea surface temperature distribution that produced realistic diurnal variations with geographical features and cyclone activity, as well as large-scale wave disturbances in the TTL. Furthermore, the regional and local-time characteristics of penetrating high clouds are important for rapid vertical transport of near-surface air into the TTL and the lower stratosphere. Consequently, we will investigate the characteristics of penetrating high clouds and compare them with observed global infrared cloud image data. However, we do not discuss water vapor variability in the TTL in the present paper because the stratospheric water vapor mixing ratio at the initial condition was set almost zero, and one-month integration was found to be not enough for water vapor to build up to a realistic concentration around the tropopause. The remainder of this paper is organized as follows. Section 2 provides the details of the MJO experiment and describes the observational data, and Section 3 presents the general characteristics of the model atmosphere obtained from the model simulations. Sections 4 and 5 contain the results and discusses their implications. We investigate the regional characteristics of deep convective clouds (section 4), and major disturbances that control the temperature of the tropopause (section 5). Finally, section 6 summarizes our findings.

2. Data Descriptions

2.1. Experimental Data

[5] In this paper we use experimental data from the NICAM simulation performed by *Miura et al.* [2007]. In the current model experiment, as in the aqua planet experiment [*Tomita et al.*, 2005; *Kubokawa et al.*, 2010], the horizontal spacing of the icosahedral grid system was set as 3.5 km and 7 km. In this study, we concentrate on the 7 km grid data because the 3.5 km grid experiment was made only for 7 days, while the 7 km grid experiment was made for one month. The number of vertical levels is 40, with the model top at ~ 38 km, resulting in a ~ 1.4 km separation between levels in and around the TTL, which is coarser than that for the aqua planet experiment (~ 0.7 km). However, we believe that the influence of deep convection and waves on the temperature variations around the tropopause can be investigated. The initial conditions of the present experiment were derived from The National Centers for Environmental Prediction (NCEP) Global Tropospheric Analysis data, and the integration was performed over 32 days, starting at 0000 UTC on 15 and December 2006. No nudging of the atmospheric observations was used during the integration. Sea surface temperature (SST) was interpolated from the weekly mean data of the Reynolds SST data set. In this study, we discard the data from the spin-up phase on the first day. Output parameters are 6-hourly snapshots of 3D winds, thermodynamic parameters, water vapor, and four condensation variables. Also, 90-minute averaged outgoing longwave radiation (OLR) data were obtained every 90 min. Other model descriptions can be found in *Miura et al.* [2007].

2.2. Observational Data

[6] Various observational data were used to evaluate the results from the NICAM model simulations. Daily OLR data from the National Oceanic and Atmospheric Administration (NOAA) polar-orbit satellites [Liebmann and Smith, 1996] with a 2.5° grid horizontal spacing were used to analyze the gross features of convective activity. Half-hourly infrared brightness temperature (T_{bb}) data from the infrared (IR) channels loaded on five geostationary satellites (the Geostationary Meteorological Satellite (GMS), the Geostationary Operation Environmental Satellites GOES-8, and GOES-10, Meteosat-7, and Meteosat-5) [Janowiak et al., 2001] were used to analyze the fine-scale convective activity. GMS data were only available hourly, and much of the data around 135°W was missing because this region is the boundary region between Meteosat-5 and GOES West measurements. NCEP/NCAR reanalysis data (NCEP1) (4 times per day, 2.5° by 2.5° horizontal resolution) [Kalnay et al., 1996], ECMWF reanalysis data (ERA-Interim) (4 times per day, 1.5° by 1.5° horizontal resolution) [Dee et al., 2011], and Japanese 25-year Reanalysis Project (JRA25) data (4 times per day, 1.25° by 1.25° horizontal resolution) [Onogi et al., 2007] were used to investigate observed temperature variations in the TTL. Finally, vertical wind data measured by the Equatorial Atmosphere Radar (EAR) at Kototabang (0.20°S , 100.32°E), Indonesia [Fukao et al., 2003; Fujiwara et al., 2003; Mega et al., 2010] were used to evaluate the NICAM vertical winds. The EAR is a 47 MHz clear-all Doppler radar that can measure vertical winds under both clear and rainy conditions. The EAR data used in this study was averaged over 90 min, with a vertical resolution of 150 m. A typical uncertainty in the vertical wind measurements at the original temporal resolution (about 80 s) is less than 0.1 m s^{-1} [Yamamoto et al., 2007].

3. General Characteristics of the Model Simulations

[7] The time-averaged fields of the circulation and thermal structure of the NICAM MJO experiment are similar to those of observation (NCEP1) (figures are not shown). In particular, NICAM reproduced the cold-point tropopause (CPT) climatology for December and January [Seidel et al., 2001]. The time-averaged horizontal pattern of OLR also generally agrees with the observations (NOAA OLR). The details of the location of active deep convection will be discussed in section 4.1.

[8] Figure 1 shows the longitude-time distribution of OLR averaged between 5°S and 5°N . Although the simulated OLR is systematically higher than the observed data (NOAA) by $\sim 20\text{ W m}^{-2}$ [see also Inoue et al., 2008, Figure 15], Figure 1 shows that the eastward propagating organized convection, with a horizontal scale of $\sim 6000\text{ km}$, is realistically simulated over the Indian Ocean and through the International Date Line. The phase speed of this organized convection is $\sim 3\text{ m s}^{-1}$, which is one of the characteristics of the MJO [Miura et al., 2007]. In contrast, the convective activity over Africa and Central America (0° – 30°E and 90°W – 30°W , respectively) is quasi-stationary. The longitudinal distribution of time averaged OLR (not shown) shows that low OLR values (less than 220 W m^{-2})

are seen over Africa (15°E – 30°E), the western Pacific (90°E – 120°E), and America (90°W – 60°W).

[9] Comparison of OLR from NICAM and NOAA, and comparison of T_{bb} from NICAM and CPC-IR (not shown), reveal that larger amounts of upper level cloud is present in the NICAM than in the real atmosphere. It has been suggested that the microphysical scheme used in the NICAM tends to produce higher amounts of ice particles in the upper troposphere [Masunaga et al., 2008; Inoue et al., 2010; Satoh et al., 2010]. These upper level clouds are not optically thick, and thus their influence on the OLR is negligible. The larger amounts of high cloud may influence the heat and water vapor budget in the TTL through radiative processes, but probably only has a limited impact on the shorter-term temperature variability that is the focus of this paper.

[10] Figure 2 shows the profiles of temperature, potential temperature, vertical temperature gradient, and the frequency distribution of cloud top height averaged between 10°S and 10°N . The cloud top height is defined as the highest (linearly interpolated) level at which the total condensates (including cloud ice, cloud water, rain, and snow) are equal to 0.01 g kg^{-1} [Kubokawa et al., 2010]. In our previous paper [Kubokawa et al., 2010], we investigated the sensitivity to the threshold value between 0.00001 g kg^{-1} and 10.0 g kg^{-1} , and found that the cloud top height does not change substantially (less than 1 km) with the values between 0.0001 g kg^{-1} and 0.1 g kg^{-1} . The temperature and the height of the CPT are 191.5 K and 16.9 km, respectively, and those of the lapse-rate tropopause are 194.0 K and 16.5 km, respectively. The values obtained for the lapse-rate tropopause are consistent with the observed zonal mean tropical lapse-rate tropopause in January (192.5 K, 16.8 km) recorded by Seidel et al. [2001]. The bottom boundary of the TTL, defined by the lapse rate minimum [e.g., Gettelman and Birner, 2007], is located at 12.0 km. Below the melting layer ($\sim 5\text{ km}$), NICAM does not simulate the stable layers which are found in the real atmosphere around 4–6 km and 2 km [e.g., Mapes, 2001; Folkins, 2009]. This may influence the low-level detrainment [Johnson et al., 1999] and thus the cloud top height statistics. There exists a local maximum in cloud top height frequency at 13–16 km. We think that this is related to anvil cirrus. When deep convection reaches the TTL, convective outflow spreads in the TTL to result in anvil cirrus formation. The 13–16 km height region corresponds to the level of maximum convective outflow. The proportion of grid points with cloud top penetrating the mean TTL bottom boundary (12.0 km), and the mean lapse-rate tropopause (16.9 km), is 20.8% and 0.53%, respectively. The tropopause overshooting frequency simulated by NICAM generally agrees with the 0.34% obtained from satellite GRAS ICESAT data in the tropics by Dessler et al. [2006]. However, this proportion changes to 0.11% and 3.69%, when we use the threshold value of 0.1 g kg^{-1} and 0.001 g kg^{-1} , respectively. The proportion does not largely change for higher threshold values, however, it is sensitive to the lower threshold values. We compare our results with those from Dessler et al. [2006], who analyzed satellite lidar data. They defined the existence of clouds using the attenuation of the emitted laser light. On the other hand, we can only use the cloud condensation concentration in g kg^{-1} in the model results; it is not easy to translate our cloud concentration threshold value into the optical depth for

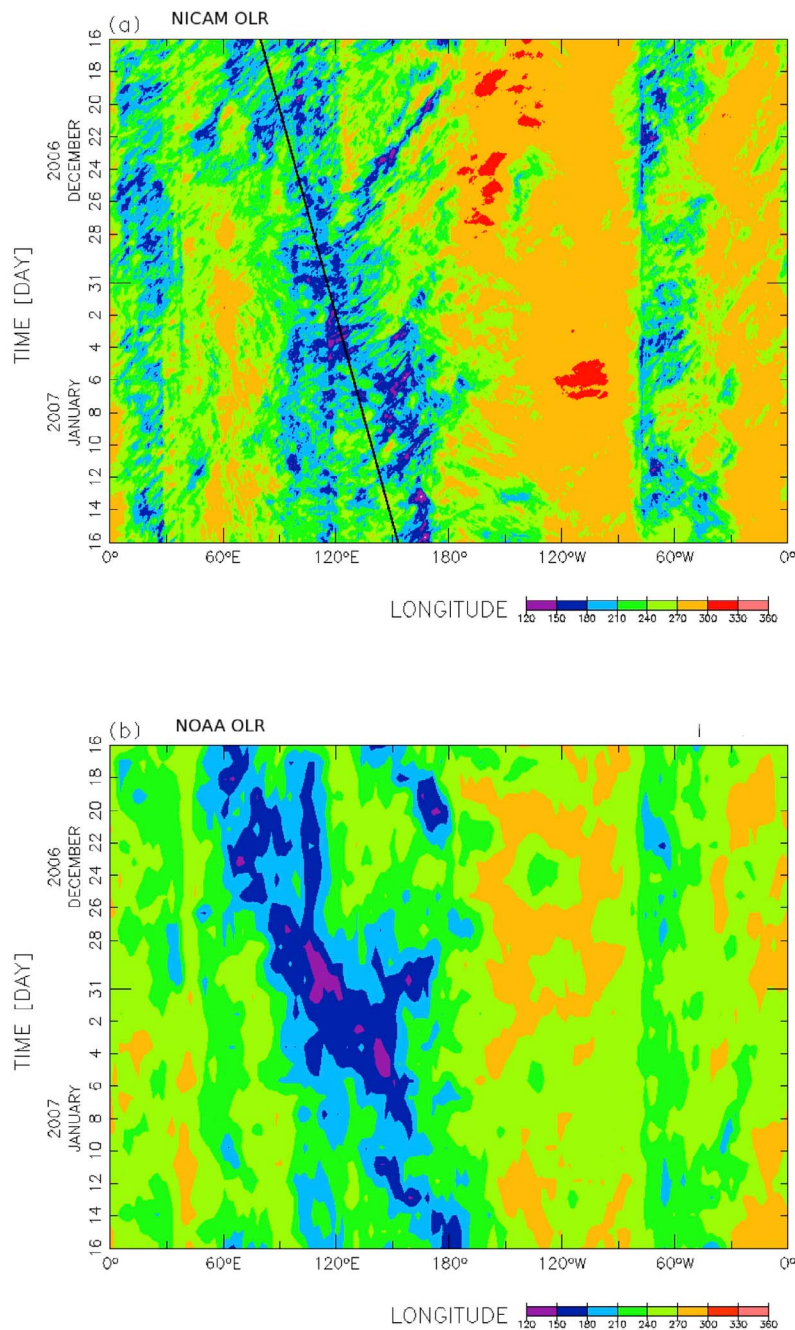


Figure 1. Longitude-time distributions of OLR averaged between 5°S and 5°N from (a) NICAM and (b) NOAA. The slanted line in Figure 1a corresponds to an eastward propagating speed of 3 m s^{-1} starting at 80°E on 16 December.

a laser light. Thus, we can make only qualitative comparison. We cannot address whether our result is an overestimation or underestimation compared with the real atmosphere, but think that the true number most probably lies between 0.11% and 3.69%. It should be noted that continental deep convection occurs at preferred hours (see Section 4) but the analysis is made using 6-hourly snapshots data. Therefore, the cloud statistics shown here may miss some very high cloud events, and the frequency in the TTL may be somewhat biased low.

[11] Figure 3 compares the frequency distribution of vertical winds from the NICAM simulation with that from the EAR observations at Kototabang (0.20°S , 100.32°E), Indonesia. For the EAR data, all available 90-minute averaged data during the December–January periods between 2001 and 2008 were used in the calculation. The amount of missing data in the upper troposphere (13–16 km) was twice that in the lower troposphere (1–10 km). The NICAM vertical wind data are six-hourly snapshots. For both data sets, the range of vertical wind speeds is mostly within $\pm 0.3\text{ m s}^{-1}$,

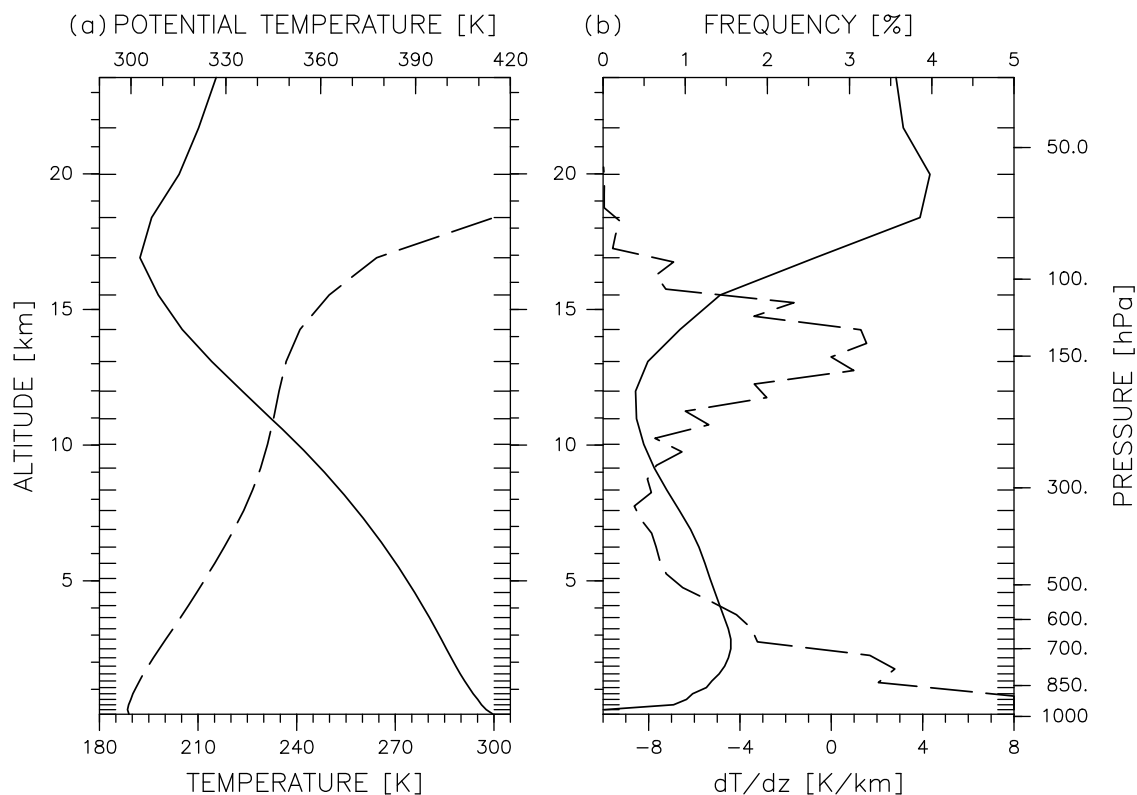


Figure 2. Average vertical distributions of (a) temperature (solid curve) and potential temperature (dashed curve), and (b) vertical temperature gradient (solid curve) and the frequency of cloud top height (dashed curve), for the region 10°S–10°N.

and those exceeding 1 m s^{-1} are extremely rare. Near the tropopause, at around 10–15 km, the frequency of light winds is lower than that at other altitude. This is probably related to the development of outflow at this level, where active vertical motion is induced. We calculated the frequency distribution of vertical mass flux (for dry air) between 5°S and 5°N (not shown). These characteristics are similar to the frequency distribution of vertical wind. Figure 4 shows the vertical profiles of mass flux for clear sky regions and deep convective regions between 30°S and 30°N. In this figure, mass fluxes for the clear-sky regions and deep convection regions almost balance. Furthermore, we can see that each mass flux change its sign around 16 km. We think that this height is the boundary of the tropic mass flux. *Folkens et al.* [1999] discussed that the bottom boundary of the TTL corresponds to the top of the Hedley circulation. In the TTL, strong vertical wind and mass flux rarely exists. The altitude of 10–15 km may be regarded as a boundary for the mass flux. Stronger downward winds prevail in the NICAM data, whereas stronger upward winds prevail in the observations at around 15 km. This difference may be caused by the limited horizontal spacing (7 km) and relatively coarse vertical resolution of the model, or different nature of the convective cloud activity in the reality and in the model whose horizontal scale is generally smaller than 7 km, or combination of these. Figure 3 also shows the frequency distribution of vertical winds from the NICAM aqua planet experiment between 5°S and 5°N. Both NICAM MJO and aqua planet data show

qualitatively similar characteristics: very strong upward winds (e.g., $\geq 6 \text{ m s}^{-1}$ and $\geq 12 \text{ m s}^{-1}$ for the MJO and aqua planet experiments, respectively) are found around 10–11 km, and the frequency curves show a decrease within the TTL. Also, relatively strong downward winds (e.g., $\leq -4 \text{ m s}^{-1}$) are found around 14–16 km in the NICAM data. This may be related to outflow in the TTL. The frequency distribution of vertical winds over the ocean is also shown in Figure 3e. The strong downward winds are merely observed compared with that of the whole 5°S–5°N (Figure 3c). This indicates that the downward winds in the upper troposphere mainly occurred over the continents.

[12] Figure 5 shows the horizontal distributions of the time-averaged altitude of the lapse-rate minimum (i.e., the bottom boundary of the TTL) and the lapse-rate tropopause. The lapse-rate minimum altitude is highest over the Indonesian maritime continent and the tropical western Pacific. The regions with higher lapse-rate minimum altitudes correspond to those with lower OLR, indicating the effects of deep convection. The distribution of tropopause altitude shows a horseshoe shaped structure over the Indian Ocean and the Pacific; the tropopause is higher in the off-equatorial regions. This structure is consistent with the observational data [e.g., *Ratnam et al.*, 2005], and is associated with the Matsuno-Gill pattern, which is the dynamical response to the tropical large-scale convective heating in the equatorial area [e.g., *Highwood and Hoskins*, 1998]. Regions of high tropopause altitude are also found over the oceans to the east

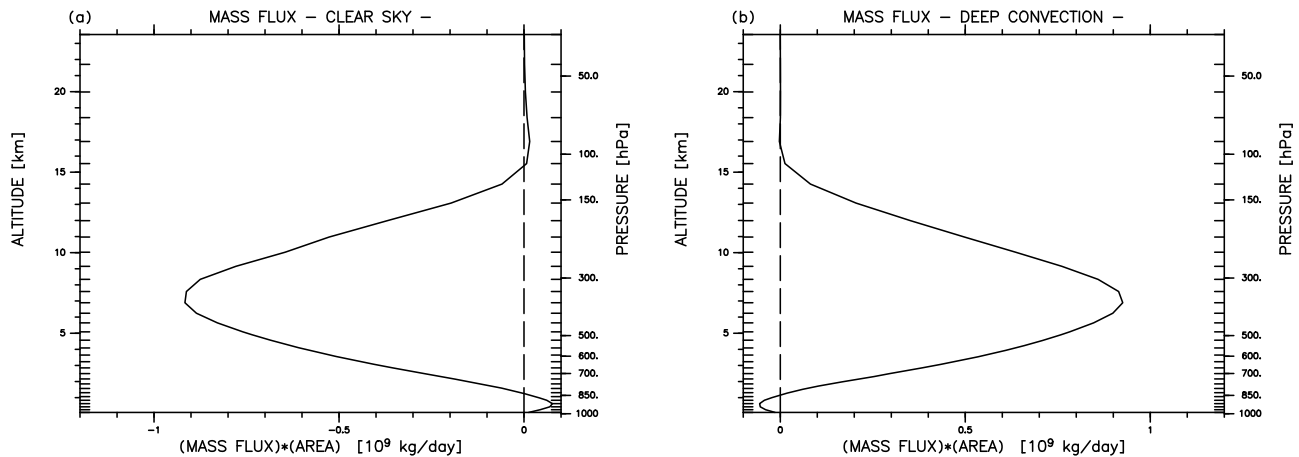


Figure 4. Vertical profiles of mass flux multiplied by area for (a) clear-sky regions and (b) deep convective regions between 30°S and 30°N. Deep convective regions are defined as grid points for which the cloud top is above 13 km and the cloud bottom is below 2.0 km.

and west of South America. This is also consistent with the observational data [Ratnam *et al.*, 2005].

[13] Figure 6 shows the standard deviation of temperature around the tropopause. Regions of high variability are found near the equator, especially over the Indonesian maritime continent. This indicates that temperature variation over the Indonesian maritime continent is controlled not only by a dynamic response to tropical large-scale convective heating, but also by short-time-scale deep convection. Over the off-equatorial regions, variations in temperature are relatively small. We will consider the local characteristics of these temperature variations in more detail in Section 5.1.

4. The Regional Characteristics of Deep Convective Activity

[14] While Sato *et al.* [2009] investigated diurnal cycles in precipitation, in this section we focus on diurnal cycles associated with deep convective activity in specific regions. We define deep convective regions as grid points where the height of the cloud top is above 16 km, and the cloud base is within 2 km of the surface. Different thresholds, such as 15 km or 17 km, generated similar results. Figure 5c shows the horizontal distribution of deep convective frequency. High frequency regions are observed over the southern African continent, southern tropical Indian Ocean, the Indonesian maritime continent through the tropical western Pacific, ITCZ, SPCZ, and the South American continent. In the following section we will investigate diurnal cycles of convective activity in three longitudinal regions (Figure 5c) namely, the Africa-Indian Ocean region (30°S–30°N, 0°–90°E),

the South American region (30°S–30°N, 90°W–0°), and the Indonesian maritime continent and western Pacific region (30°S–30°N, 90°E–180°).

4.1. The Africa-Indian Ocean Region

[15] Figure 7 shows areas of high, deep convective activity within the Africa-Indian Ocean region, where the cloud top extends above both the lapse-rate tropopause (16 km) and the bottom boundary of the TTL defined by the local lapse-rate minimum. Figure 7d shows the observed high frequency areas from the CPC-IR data, with a threshold value of 200.69 K. This threshold value corresponds to the average temperature at 15 km (119.7 hPa) between 30°S and 30°N in the NCEP reanalysis data. Sherwood *et al.* [2004] indicate that cloud top heights estimated from geostationary infrared satellite data are ~ 1 km lower than those estimated from ground-based lidar. Therefore, the CPC-IR panel may be compared with the NICAM 16 km threshold panel. Very high, deep convection in the NICAM is observed mainly in the southern part of the African continent (25°S–15°S, 15°E–30°E; area (1) in Figure 7a), while moderately deep convection that reaches the lapse-rate minimum is often observed a little further north (10°S–equator) (Figure 7c). High frequency regions are also found around the south of Madagascar (area (2) in Figure 7a) associated with organized convective clouds with a horizontal extent of ~ 500 km (particularly between 26–28 December 2006). In the south western tropical Indian Ocean (10°S, 60°E; area (3) in Figure 7a), high frequency regions are associated with tropical cyclone Bond, which developed around 18 December 2006 [Fudeyasu *et al.*, 2008]. High frequency regions in

Figure 3. Frequency distributions of vertical wind (a) at the grid point (0.24°S, 100.30°E) near the EAR site using the NICAM-MJO experiment data, (b) at the EAR site (0.24°S, 100.30°E) using all available EAR data for December–January between 2001 and 2008, (c) in the region 5°S–5°N using the NICAM-MJO experimental data, (d) in the region 5°S–5°N using the NICAM aqua planet experimental data (reproduced from Figure 8 of Kubokawa *et al.* [2010]), and (e) in the region 5°S–5°N, 180°–100°W, but only over the ocean, using the NICAM-MJO experimental data. Contours represent the frequency of grid points in each $\Delta w = 0.1 \text{ m s}^{-1}$ bin at each altitude level (shown as inner ticks in each panel). Note that while 3.5 km horizontal spacing data is used in Figure 3d, 7.0 km horizontal spacing data is used in Figures 3a, 3c, and 3e.

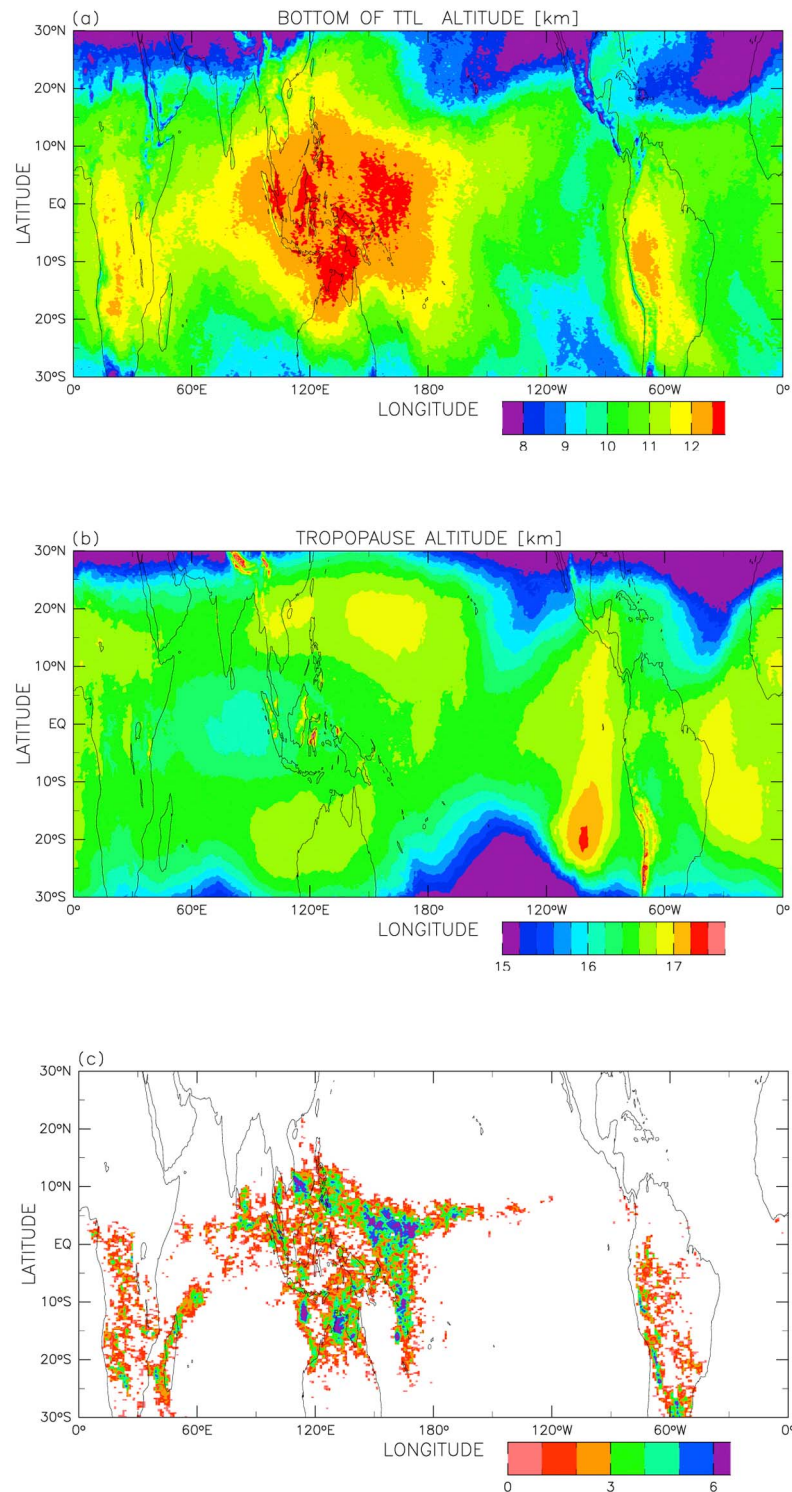


Figure 5. Horizontal distributions of time-averaged altitude of (a) lapse-rate minimum (the TTL bottom), and (b) lapse-rate tropopause. (c) Horizontal distribution of deep convective frequency (expressed as a percentage). Deep convection is defined as grid points where the cloud top is located above 16 km and the cloud bottom is located within 2 km of the surface. Cloud is defined as total condensate $\geq 0.01 \text{ g kg}^{-1}$.

the eastern equatorial Indian Ocean (area (4) in Figure 7a) are associated with the MJO convection.

[16] High frequency regions in the CPC-IR data occur over the southern African continent, south western tropical

Indian Ocean (10°S, 60°E), and eastern equatorial Indian Ocean, showing that the NICAM results are generally valid. Over the southern African continent (area (1) in Figure 7a),

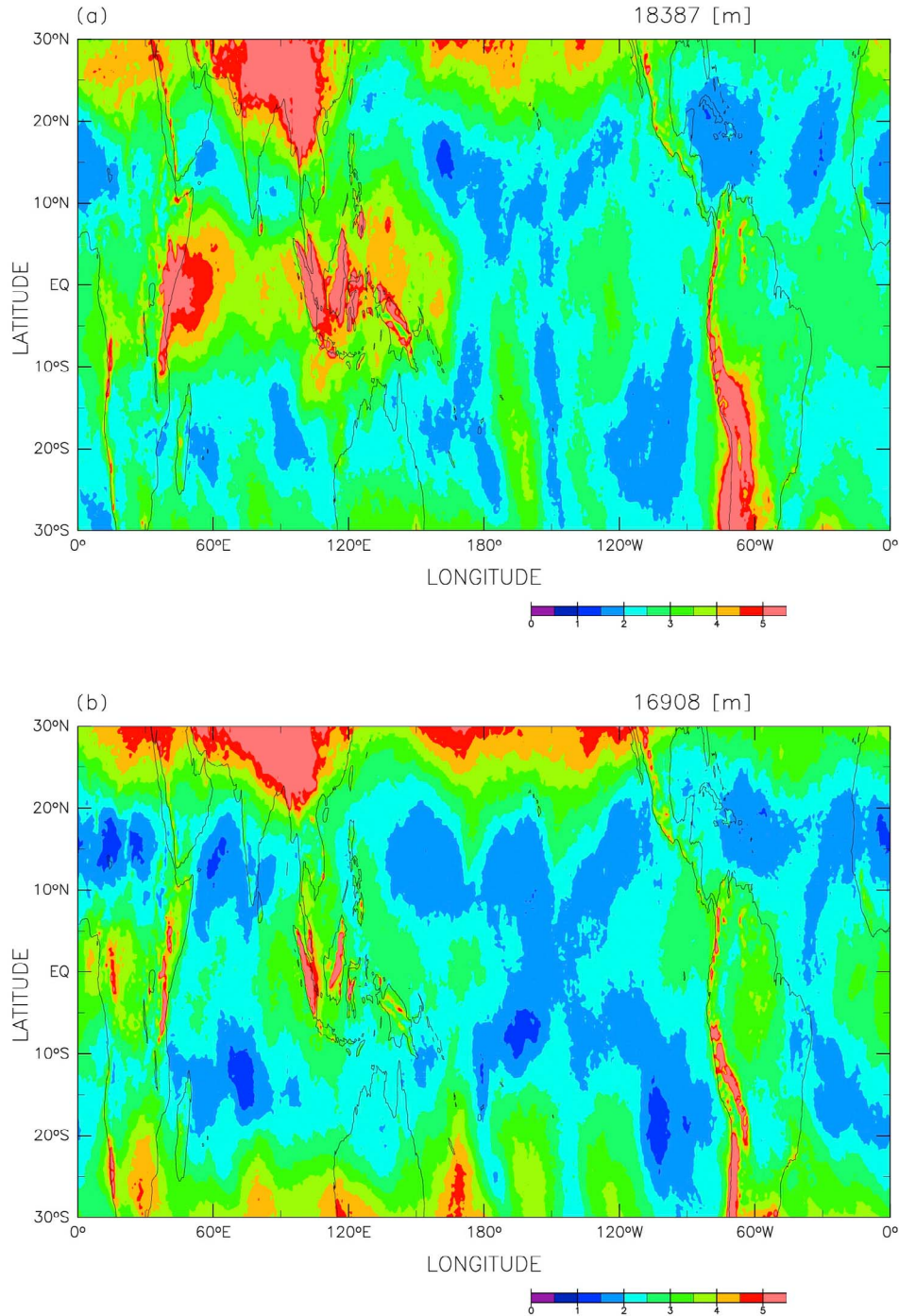


Figure 6. Horizontal distributions of the standard deviation of temperature at (a) 18.4 km and (b) 16.9 km.

deep convective activity shows a marked local dependence in both the NICAM and the observed atmospheric data.

[17] Figure 7 also shows a diurnal time series of deep convective activity over the southern African continent (30°S–15°S, 15°E–30°E), the area enclosed by a rectangle in Figure 7b. Here, we use the 90-minute interval OLR from the NICAM data, and the half-hourly T_{bb} data from the CPC-IR data; therefore, the comparison is only qualitative. For the CPC-IR data, we again used 200.69 K as the

threshold value for deep convective activity, while for the NICAM OLR data, we used 137.5 W m^{-2} . This was determined using the histograms of the CPC-IR T_{bb} data and the NICAM OLR data such that the summation of high-cloud frequency for CPC-IR $T_{bb} \leq 200.69 \text{ K}$ (3.38%) becomes equal to that for the NICAM OLR threshold value. The high-cloud frequency is at a minimum between 0600 and 0900 UT (0700 and 1000 LT), and increases after 0900 UT (1000 LT) for both the NICAM and CPC-IR data. For CPC-IR, the

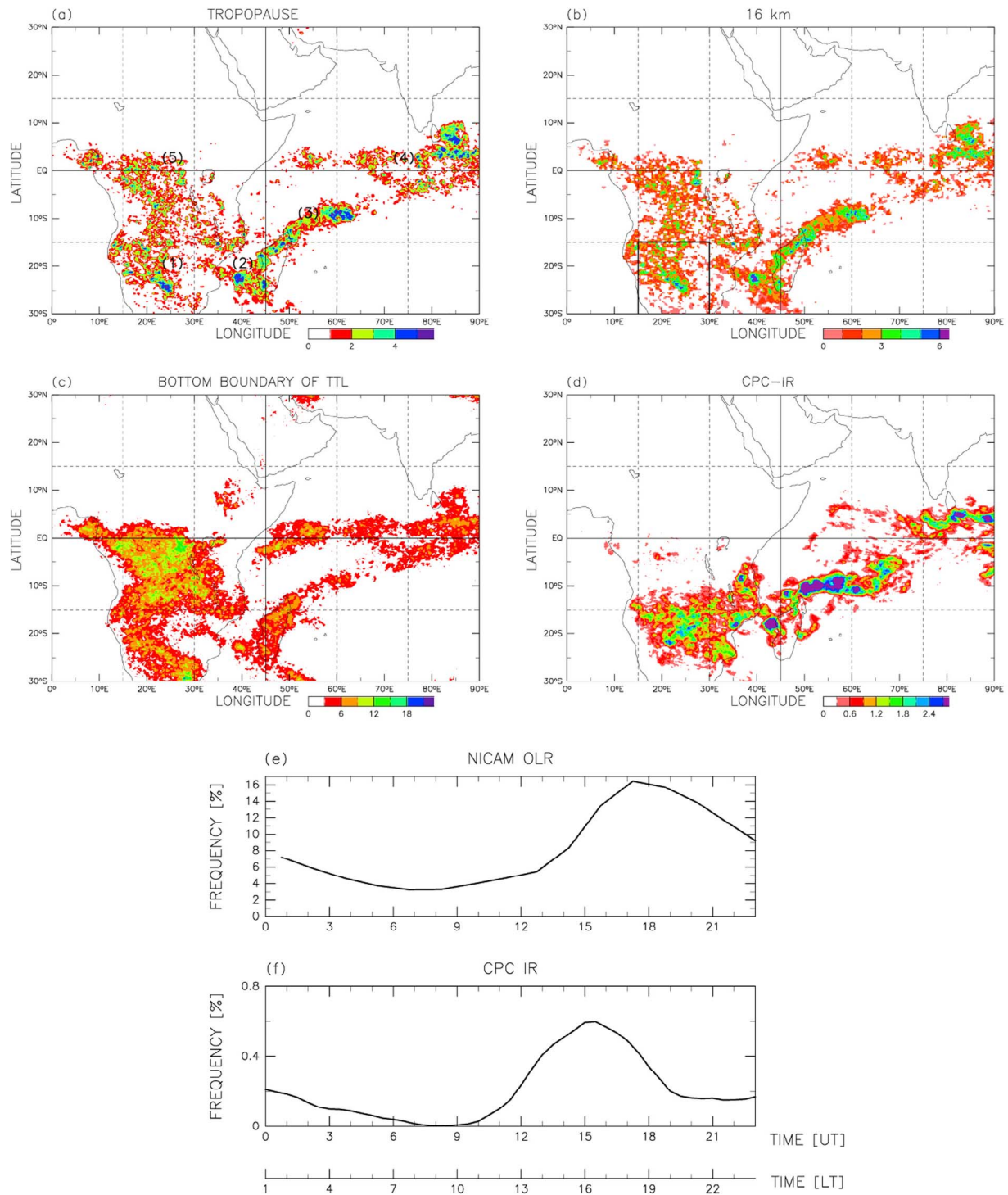


Figure 7. Horizontal distributions of deep convective frequency (expressed as a percentage). Deep convection is defined as grid points where the cloud top is located (a) above the local lapse-rate tropopause, (b) above 16 km, and (c) above the local lapse-rate minimum. For Figures 7a–7c, an additional condition that the cloud base is located within 2 km of the surface is applied. (d) The deep convective frequency using CPC-IR data with a threshold value of 200.67 K (see text for details). See text for the numbers (1)–(5) in Figure 7a. Diurnal time series of deep convective frequency in the area (30°S–15°S, 15°E–30°E) during 16 December 2006 to 15 January 2007 using (e) NICAM OLR data and (f) CPC-IR T_{bb} data. The threshold values used here are 137.5 W m^{-2} for Figure 7e and 200.69 K for Figure 7f. Note that 12 UT corresponds to 13–14 local time (LT) in this region.

frequency reaches its maximum value around 1500 UT (1600 LT), while for the NICAM, the maximum frequency is somewhat later, around 1700 UT (1800 LT). The maximum frequency values are quite different between Figures 7e and 7f. This is probably because the simulated cloud activity is different from that in the real atmosphere particularly in the relevant region. The factors for the different cloud activity include (1) the issues in the choice of microphysical scheme discussed in Section 3, and (2) the horizontal grid of 7 km for the simulation discussed in this paper (note that the observational data shown here have the horizontal resolution of 4 km). We also note the fact that deep convection tends to persist over the continents particularly near high mountains in this simulation.

4.2. The South American Region

[18] Figure 8 shows areas of high, deep convective activity within the South American region. Very high clouds in the NICAM developed mainly over the southern South American continent, (25°S–15°S, 70°W–60°W) (area (1) in Figure 8b), (30°S–25°S, 70°W–60°W) (area (2) in Figure 8b), and around (10°S, 75°W). Over the Atlantic Ocean, almost no deep convective clouds developed that reached the lapse-rate tropopause or 16 km level. High frequency regions of the CPC-IR data are mostly confined to the south of the South American continent (30°S–15°S, 65°W–50°W). These high clouds were mainly associated with transient disturbances with a \sim 7-day period (not shown). Simulated high clouds are over-generated along the Andes in general.

[19] Figure 8 also shows the diurnal time series of deep convective activity over the southern South American continent (areas (1) and (2) in Figure 8b). High-cloud frequency is at a minimum between 1200 and 1500 UT (0800 and 1100 LT), and increases after 1500 UT (1100 LT) in both the NICAM and CPC-IR data. For the CPC-IR, the maximum frequency occurs around 2000 UT (1600 LT), while for the NICAM, the maximum occurs around 0000 UT (2000 LT). The NICAM maximum frequency is around four hours later than that in the observed data. *Sato et al.* [2009] show that the precipitation maximum in the NICAM MJO 7 km grid data is 3 hours later than that of the Tropical Rainfall Measuring Mission (TRMM) results over South America. They showed that the time difference becomes larger as the horizontal resolution becomes coarser. They speculated that the phase lag of the simulated diurnal cycle of deep convection is related to boundary layer processes, which are very important for the initiation of deep convection.

4.3. The Indonesian Maritime Continent and Western Pacific Region

[20] Figure 9 shows areas of high, deep convective activity over the Indonesian maritime continent and western Pacific. The high frequency regions are over the southern South China Sea, around northern Sumatra, near the southern coast of Java, over northern Australia, in the ITCZ, and in the SPCZ; this is generally consistent with the CPC-IR results, except for some differences over New Guinea. For both the NICAM and CPC-IR data, high frequency regions south of Java are associated with tropical storm Isobel [*Fudeyasu et al.*, 2008]. High frequency regions in northern Australia in the NICAM data are associated with a convective system

with a horizontal extent of \sim 1000 km during the active phase of MJO; this convective system is not seen in the CPC-IR data. In the ITCZ and SPCZ in the NICAM data, high clouds are associated with westward propagating disturbances with a horizontal extent of \sim 500 km, and a period of two days. In the ITCZ and SPCZ in the CPC-IR data, high clouds are also associated with westward propagating disturbances with a period of two days. However, the horizontal scale of these disturbances was \sim 100 km.

[21] Figure 9 also shows the diurnal time series of deep convective activity over the southern South China Sea (8°N–12°N, 110°E–115°E; area (1) in Figure 9b), north of Java (7°S–4°S, 110°E–118°E; area (2)), the ITCZ (7°S–4°S, 150°E–165°E; area (3)), and the SPCZ (12°S–8°S, 163°E–167°E; area (4)). As noted in Section 2.2, a significant amount of data is missing from the CPC-IR data over the Pacific; and this explains the noisy curves in Figure 9f. From the NICAM data, over the seas around large islands in areas (1)–(2), the frequency reaches a maximum (minimum) around 0600 UT (1600 UT), indicating the local afternoon (midnight) maximum (minimum). From the CPC-IR data, in area (1), high (low) frequency is seen around 0500 UT (1200 UT). The time of local maximum in the NICAM is slightly later than that in the CPC-IR data, but the time of the local minimum is quite different. High (low) frequency in area (2) occurs around 0300 UT (0900 UT) in the CPC-IR data, slightly earlier than that in area (1). The time difference between areas (1) and (2) was present in the NICAM data. The local-noon maximum in the NICAM is consistent with atmospheric observations. Over the ITCZ in area (3), the frequency maximum (minimum) is seen around 0400 UT (1000 UT), indicating the local afternoon (evening) maximum (minimum). The local time dependence in the SPCZ is almost the same as that in the ITCZ. In area (3), high (low) frequency is found around 2000 UT (0600 UT); the local time dependence in the NICAM is not consistent with atmospheric observations. In area (4), high frequency occurs between 0600 UT and 2000 UT. The variation in the diurnal cycle in the NICAM is clearer than that in the observational data. In summary, the NICAM simulates clear diurnal cycles in deep convective activity reasonably well; however, the frequency maximum over land in the NICAM occurs \sim 2 hours later than in the observational data, and the frequency maximum over the oceans is delayed even further (\sim 9 hours) compared with the atmospheric observations. This is in part due to insufficient horizontal resolution (7 km), and also because of the microphysical scheme used in the NICAM. The present model simulations shows a larger amount of ice particles in the upper troposphere, which is also thought to be caused by the microphysical scheme as discussed in section 3 [*Masunaga et al.*, 2008; *Inoue et al.*, 2010; *Satoh et al.*, 2010].

[22] In this section, we have investigated the regional characteristics of deep convective activity and compared them with empirical data from atmospheric observations. It was shown that the geographical distribution and diurnal cycles of active deep convection are realistically simulated by the NICAM, although a time lag of convective activity exists between the NICAM and the observations. As we have confirmed that the NICAM simulation reproduces many of the characteristics of deep convective activity, such

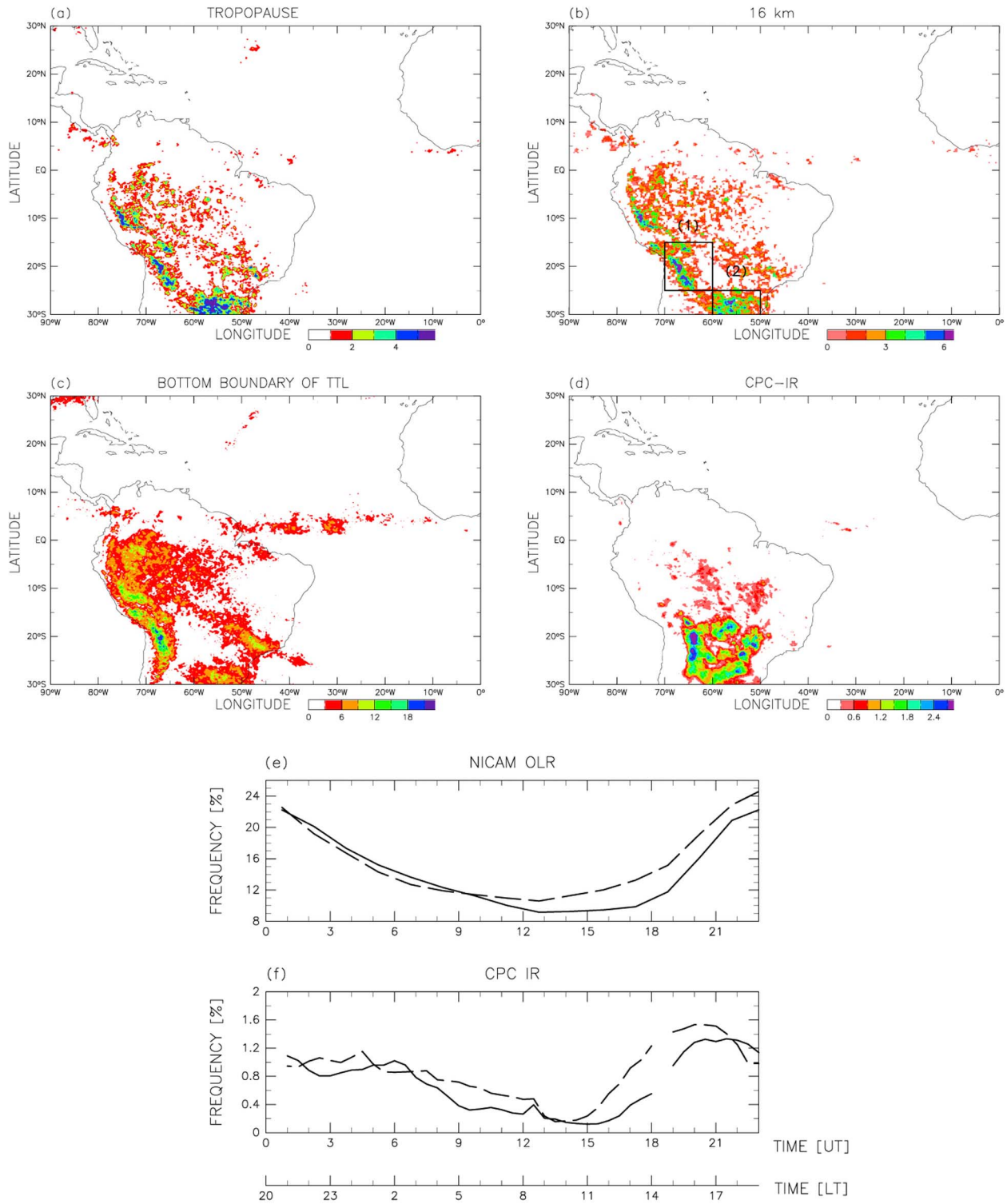


Figure 8. As for Figure 7, but for the South American region. Solid and dashed curves in Figures 8a and 8f indicate the diurnal time series for the areas (1) (25°S–15°S,70°W–60°W) and (2) (30°S–25°S,70°W–60°W), respectively, shown in Figure 8b. Note that 12 UT corresponds to 8–9 LT in this region.

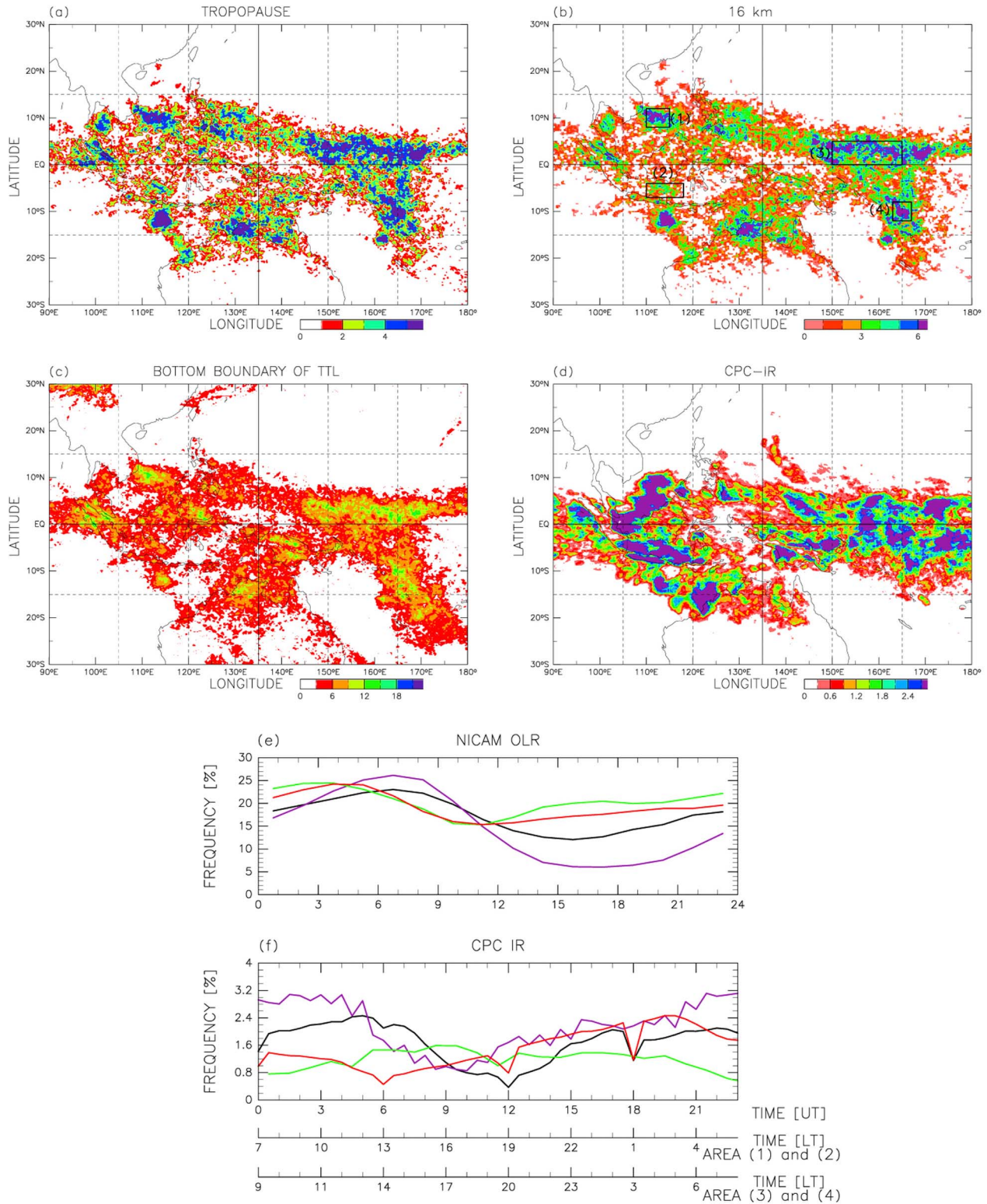


Figure 9. As for Figure 7, but for the Indonesian maritime continent and western Pacific region. Black, purple, red and green curves in Figures 9e and 9f correspond to the area (1) (8°N–12°N, 110°E–115°E), (2) (7°S–4°S, 110°E–118°E), (3) (7°S–4°S, 150°E–165°E), and, (4) (12°S–8°S, 163°E–167°E), respectively, in Figure 9b. Note that 00 UT corresponds to 7–8 LT in areas (1) and (2), but 9–11 LT in areas (3) and (4).

Table 1. The Location and Value of Maximum Standard Deviation at Each Regions

Name	Location	Value
Africa	38.1°E, 5.4°S	8.75 K
Sumatra	99.6°E, 2.0°N	11.76 K
Kalimantan	116.8°E, 1.3°N	10.46 K
Sulawesi	120.5°E, 2.4°S	9.12 K
Andes	76.3°W, 9.7°S	9.00 K
Tibet	97.7°E, 27.7°N	16.46 K

as its frequency, location, and diurnal cycles (at least qualitatively), we can now use the NICAM data to consider temperature variations in the TTL.

5. Temperature Variations in the TTL

[23] We will now investigate temperature variations around the tropopause associated with (1) local-to-regional deep convective activity (as discussed in the previous section), (2) tropical cyclones, and (3) large-scale disturbances (equatorial Kelvin waves). We will then estimate their relative contribution in terms of dehydration capability.

5.1. The Regional Characteristics of Tropopause Temperature Variations

[24] As shown in the previous section, deep convective activity has regional characteristics. If such deep convective activity has a large influence on the temperature variations around the tropopause, water vapor entering the stratosphere may be controlled in part in specific regions. Figure 6 shows the standard deviation of temperature around the tropopause. Regions with large standard deviations are found over eastern equatorial Africa (40°E–50°E, around the equator), over the Indonesian maritime continent (Sumatra; Kalimantan; Sulawesi), over the Andes, and over Tibet (70°E–105°E, 20°N–30°N). Table 1 shows the location and value of maximum standard deviation at each regions. Figure 10 shows the time-altitude distributions of temperature around the tropopause at the six grid points. Over eastern equatorial Africa (Figure 10a), deep convective activity is not seen (see Figure 7). In this region, low temperatures occur continuously around the tropopause between 22 December and 31 December 2006. These low temperatures have a horizontal (zonal and meridional) extent of ~1000 km (not shown) in this region. Over the Indonesian maritime continent (Sumatra, Kalimantan, and Sulawesi), large, low-frequency temperature variations are found at 16.9 km. Over Sumatra, low temperatures persist until 31 December 2006. Over Kalimantan (see also Figure 11) and Sulawesi, low temperatures occur between 31 December 2006 and 10 January 2007. These temperature variations have an amplitude of up to ~20 K, and are associated with large-scale eastward-propagating waves that will be discussed in Section 5.3 (note that the amplitude may be too large compared with previous observations; see also Section 5.3). In these regions, diurnal variations in temperature are superimposed on the large, low-frequency variations. The amplitude of the diurnal cycle reaches as high as ~10 K. The local deep convective activity is the major factor in the diurnal variations. Over the Andes, two large-amplitude events occur around 17–19 December

2006 and 3–4 January 2007. The horizontal range of these temperature variations was less than 500 km. Over Tibet, temperature variations with a period of a week make a major contribution to the large standard deviation. Diurnal variations of ~10 K also make some contributions there. *Seidel et al.* [2005] and *Fujiwara et al.* [2009] analyzed radiosonde data from the tropical western Pacific and show that the diurnal amplitude at the tropopause is 0.5–1.5 K. *Jain et al.* [2006] analyzed radiosonde data from southern India and show the diurnal amplitude of up to ~5 K. *Alexander and Tsuda* [2008] analyzed radiosonde data from South east Asia (mostly western Indonesia) and northern Australia, and show that the amplitude of the diurnal tide is 0.5–1.5 K around the tropopause. The much larger amplitudes found in the NICAM may in part be due to the relatively coarse vertical resolution (~1.4 km) in the TTL in this model simulations. Although the amplitude values should be viewed with caution, and may be much greater than the actual values, the NICAM results suggest that diurnal variations in temperature in the TTL due to deep convective activity may contribute to dehydration in certain regions.

5.2. Tropical Cyclones

[25] *Fudeyasu et al.* [2008] report that two tropical cyclones over the Indian Ocean, Bond (first observed on 18 December 2006), and Isobel (first observed on 29 December 2006), were realistically simulated in this NICAM MJO experiment. We have already shown that some deep convective clouds reach the tropopause over these two cyclones (Figures 7a and 9a). Consequently, it is possible that these cyclones have a significant affect on temperature variations around the tropopause.

[26] Figure 12 shows the horizontal distributions of cloud top height and temperature at 16.9 km, where, and when, tropical cyclone Bond was active. The center of tropical cyclone Bond was observed at 9°S, 58°E on 19 December 2006. Bond propagated south-westward, and weakened until 22 December. On 19 December, low temperatures of less than 190 K (192.3 K for 10°S–10°N average) were observed over the core of Bond. The temperature was as low as 184.1 K. The zonal extent of the low temperature region of less than 190 K was ~500 km. After 20 December, the low temperature region tended to be dissipated and spread. This was caused by the propagation of gravity waves excited by tropical cyclone Bond, which is discussed later. On 22 December, the low temperature region of less than 190 K had extended to 1000 km in zonal extent. Tropical cyclone Bond had dissipated by 22 December, and the low temperature region associated with Bond had dissipated completely by 24 December.

[27] Figure 13 shows the horizontal distributions of the anomaly fields of temperature and zonal wind by applying a spatial band-pass filter of 4–10 degrees. We applied a filter to show the characteristics of waves more clearly. The minimum temperature of –3.6 K is observed at 8°S, 58°E at 12 LT on 19 December 2006. This low temperature region is directly associated with the deep convection of Bond, and propagates south-westward. At 12 LT on 19 December 2006, we see a horizontal wind divergence around tropical cyclone Bond. At 18 LT on 19 December 2006, the warm-cold temperature anomalies, and east–west wind anomalies, spread spatially, with a circular form, from tropical cyclone

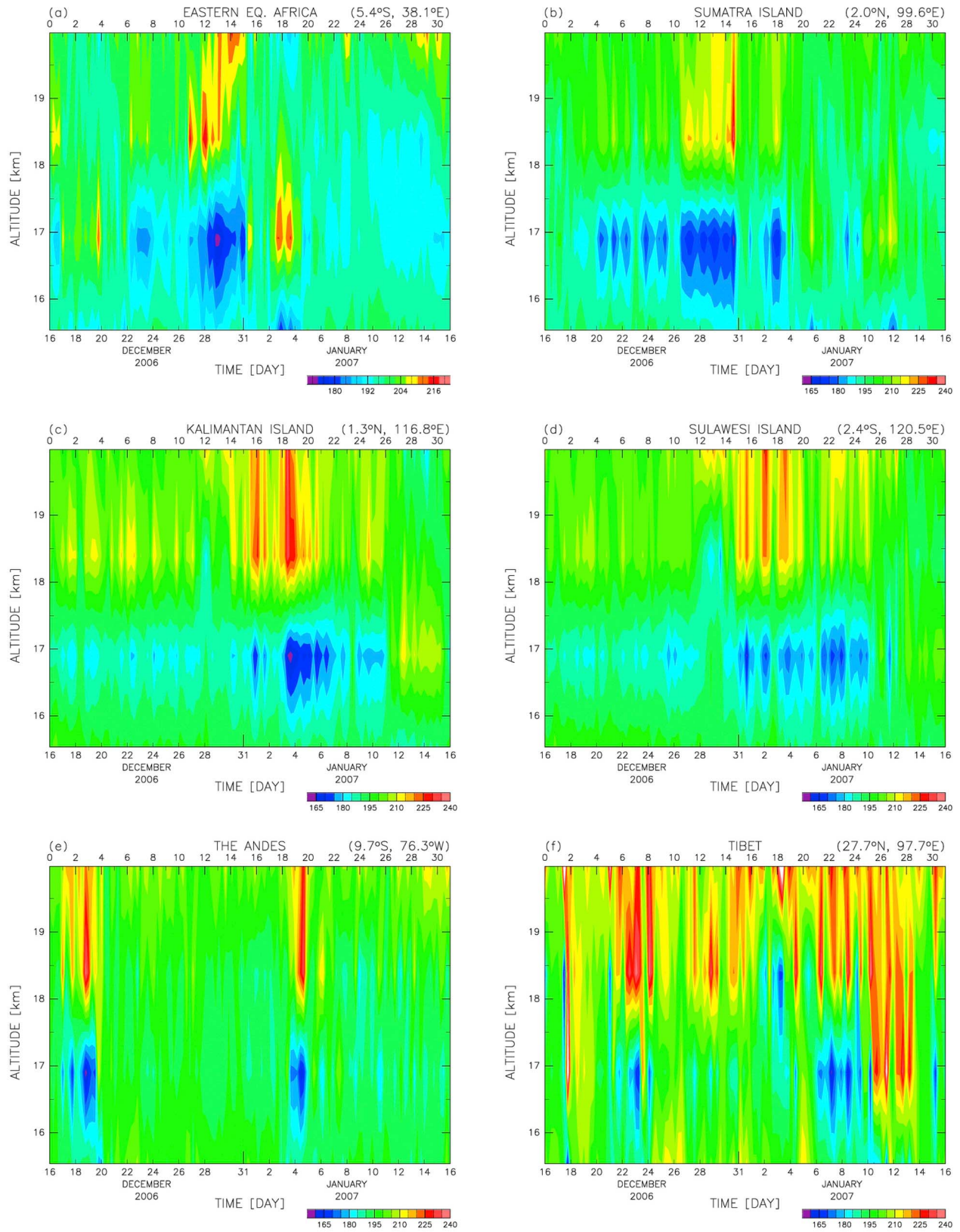


Figure 10. Time-altitude distributions of temperature at (a) eastern equatorial Africa (5.4°S, 38.1°E), (b) Sumatra (2.0°N, 99.6°E), (c) Kalimantan (1.3°N, 116.8°E), (d) Sulawesi (2.4°S, 120.5°E), (e) the Andes (9.7°S, 76.3°W), and (f) Tibet (27.7°N, 97.7°E). Note different shading in each panel.

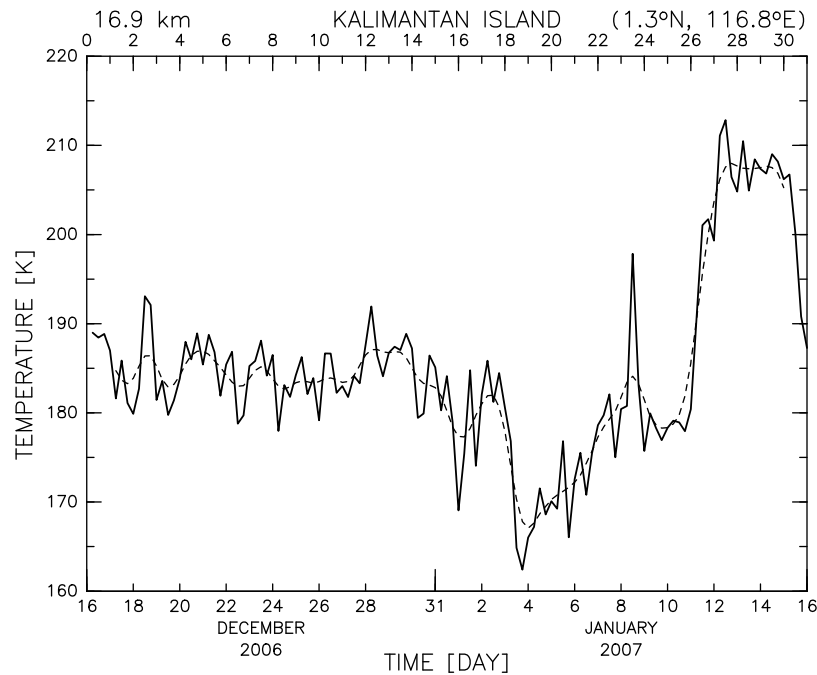


Figure 11. Time series of temperature at 16.9 km at Kalimantan (1.3°N, 116.8°E). Dotted curve shows a ~ 2 -day running average.

Bond. These anomalies reach ~ 1000 km from the center of Bond (warm anomalies have reached as far as 45°E, 7°S). After 12 LT on 19 December 2006, the wave patterns are clearly seen in both temperature and zonal wind anomaly fields, especially in the region south-eastward of Bond. At 12 LT on 19 December 2006, wave patterns in temperature and zonal wind anomalies show a quadratic phase difference along the thick dotted line in the figure. This phase relationship indicates that the disturbances are gravity waves with a horizontal wavelength of ~ 600 km. Also, hodograph analysis shows the rotating characteristics of gravity waves (not shown). i.e., a counter-clockwise with height indicating the upward energy propagation. Figure 14 shows a vertical cross-section of temperature and zonal wind anomalies around the tropopause at 12 LT on 20 December 2006. Above 16 km, warm and cold anomalies show a southeastward upward tilt, while those below 16 km show a southeastward downward tilt, indicating energy propagation from the 16 km level. The vertical wavelength was estimated to be ~ 3 km. The amplitude of the temperature and zonal wind components is ~ 1.9 K, ~ 6 m s $^{-1}$, respectively. The period relative to the ground was estimated to be ~ 8.5 hours from the dispersion relationship of gravity waves: $\omega = k \left[v - \frac{N}{m} \right]$.

[28] For tropical cyclone Isobel, the horizontal distribution of cloud top height and temperature at 16.9 km is shown in Figure 15. The center of Isobel was at 12°S, 115°E on 31 December 2006. Some other deep convective clouds are seen to the north of Australia, which were located within the active phases of the MJO (Figure 1a). The cloud top height of Isobel and other clouds often reaches the tropopause (see Figure 9a). Isobel propagated southeastward and became weaker after 4 January 2007. On 31 December 2006, low temperatures of less than 190 K were prominent

over the region north of 15°S. This was associated with the MJO which will be discussed in the next section. Very low temperatures of less than 184 K were observed around the region where active deep convective clouds near Isobel and the MJO developed. On 2 January 2007, a large-scale low temperature region of less than 182 K was observed between 15°S and 5°S and 104°E and 114°E. This low temperature region was detached from Isobel. The relationship between this low temperature region and the tropical cyclone is not clear, but gravity wave generation may have been involved. After 3 January 2007, this low temperature region propagated southwestward and had dissipated by 5 January 2007.

[29] We also examined the 100-hPa temperature variations associated with these two tropical cyclones using three sources of reanalysis data, namely, NCEP1, ERA-Interim, and JRA25. Although the corresponding signals in the 100-hPa temperature are not very clearly seen in all three data sets, the temperature might be 2–4 K lower than the surroundings in both cases. It is possible that the reanalysis data are not particularly effective at capturing the influence of tropical cyclones. *Danielsen* [1993] shows temperature profiles above tropical cyclones; the tropopause temperature above tropical cyclones can be ~ 7 K colder than the surroundings in the real atmosphere. In summary, we have quantified the spatial extent (~ 500 km) of the TTL low temperature regions (~ 6 -K drop) associated with tropical cyclones. Considering their life span of 4–6 days, these tropical cyclones have the potential to contribute to dehydration processes in the TTL.

5.3. Equatorial Kelvin Waves and MJO

[30] Figures 16 and 17 show the longitude-time distributions of temperature and zonal wind around the tropopause averaged between 5°S and 5°N at 16.9 and 18.4 km. The

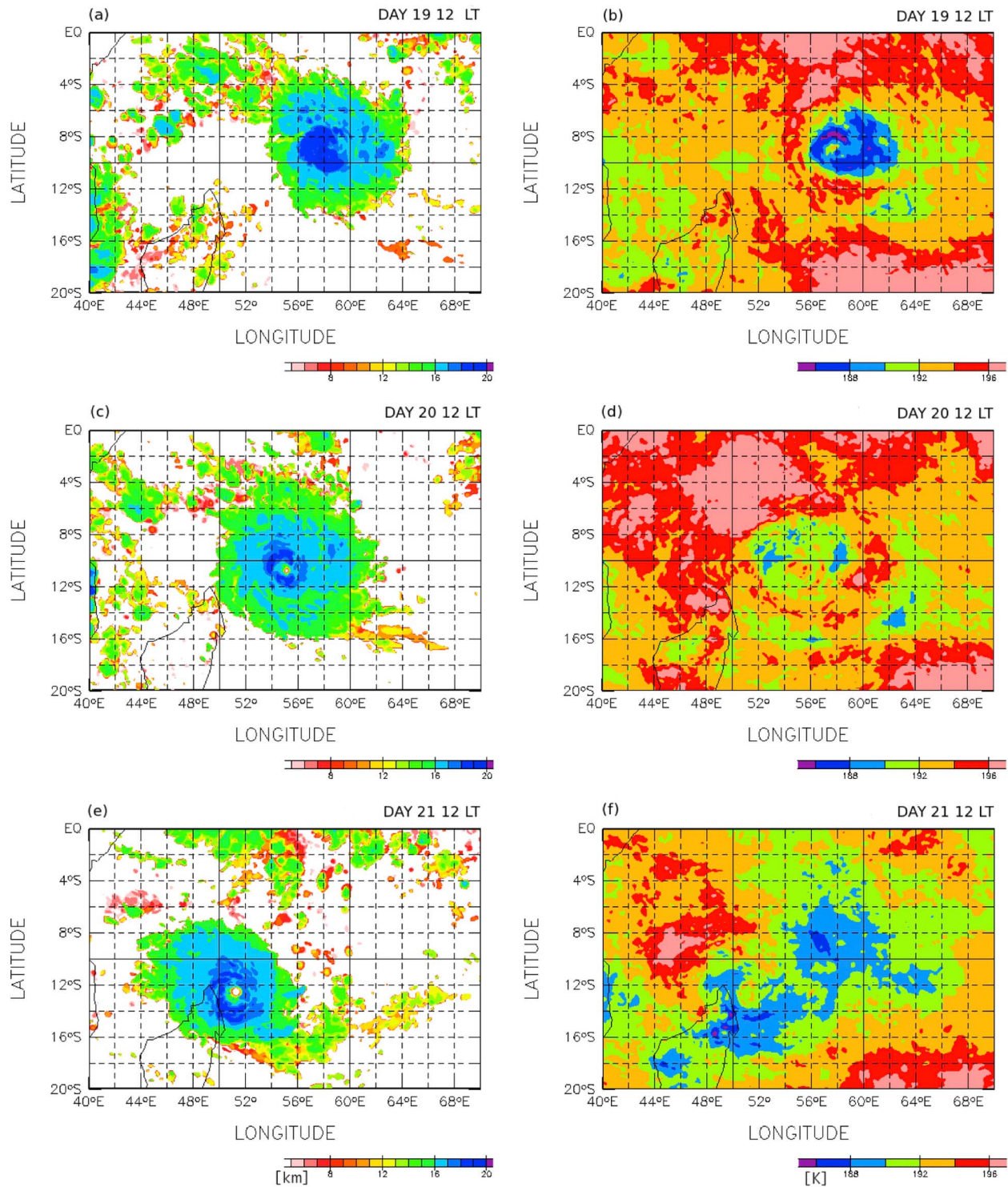


Figure 12. Horizontal distributions of (a, c, e) cloud top height and (b, d, f) temperature at 16.9 km over tropical cyclone Bond at 12 LT on 19, 20, and 21 December 2006 using NICAM data.

zonal-time averaged temperatures at 16.9 and 18.4 km are 192.2 K and 196.0 K, respectively, and the temperature anomaly pattern are roughly the same for the 20°S–20°N average (not shown). A slow (3 m s^{-1}), eastward propagating low-temperature signal (less than 190 K) is seen from the

Indian Ocean to the International Date Line at 16.9 km. Similar eastward propagating zonal wind signals are also observed at 16.9 km. A quadratic phase difference is clearly seen between the temperature and zonal wind fields around the tropopause. These signals are associated with the MJO

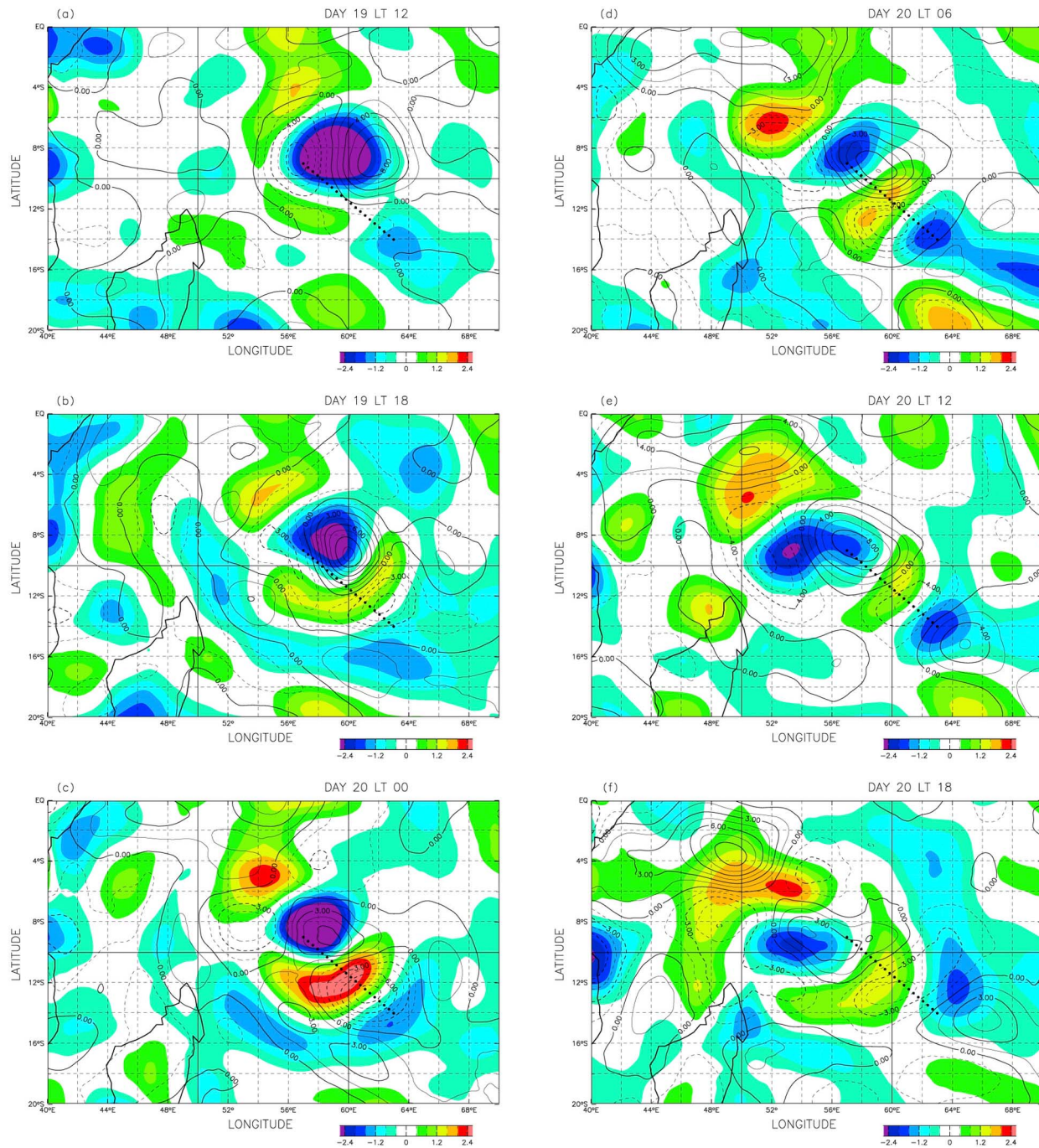


Figure 13. Horizontal distributions of temperature (color) and zonal wind anomaly (contour) at 16.9 km from (a) 06 LT on 19 December 2006 to (f) 18 LT on 20 December 2006, with (b–e) 6-hour intervals. A band-pass filter of 4–10 degrees has been applied. The slanted dotted line corresponds to (57°E, 9°S)–(63°E, 14°S).

convection shown in Figure 1 (see the slanted solid lines in Figures 1 and 16). Similar tropopause temperature signals are also observed in the NCEP1 reanalysis data. This indicates that the NICAM simulates large-scale temperature signals in the real atmosphere reasonably well. The low temperature region at 16.9 km in the NICAM data is located

to the east of the corresponding low temperature regions at 15.5 km, the next model level, indicating an eastward phase tilt with height. At 18.4 km, a warm region is seen over the MJO convection. Using the wave parameters, we confirmed that the slow eastward-propagating signal can be regarded as equatorial Kelvin waves with a strong easterly background

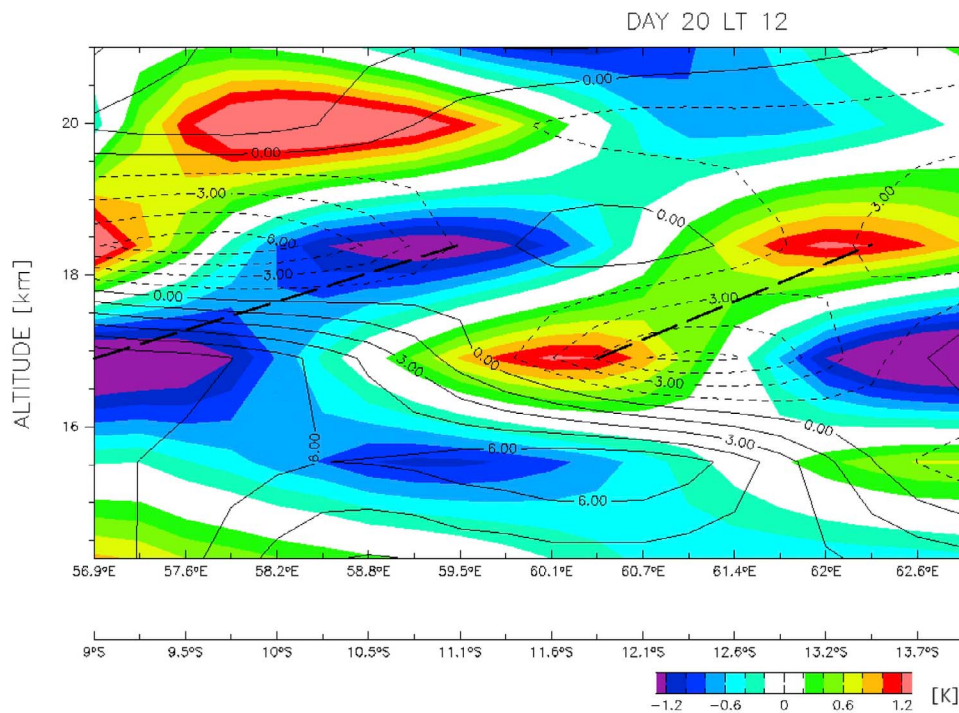


Figure 14. A horizontal-vertical distribution of temperature and zonal wind anomalies around the tropopause (14.2 km–21 km) at 12 LT on 20 December 2006. The horizontal axis corresponds to the thick dotted line in Figure 13. The two slanted dotted lines in this figure correspond to those from (left) 56.9°E, 9°S, 16.9 km to 59.5°E, 11.1°S, 18.4 km, and (right) 60.4°E, 11.9°S, 16.9 km to 62.3°E, 13.5°S, 18.4 km, respectively.

flow. Previous studies of tropopause disturbances associated with the MJO [e.g., Madden and Julian, 1972; Knutson and Weickmann, 1987; Nishi, 1989; Hendon and Salby, 1994; Mote et al., 2000; Fujiwara and Takahashi, 2001; Suzuki and Shiotani, 2008; Suzuki et al., 2010] show that Kelvin waves generated by the MJO convection largely affect the temperature field around the tropopause. In this model simulations, Kelvin waves similarly control the temperature field around the tropopause. The zonal scale of this low temperature region is as large as $\sim 10,000$ km. The temperature amplitude is up to ~ 6 K, even when averaged between 5°S and 5°N . Over Kalimantan, the amplitude is up to ~ 20 K, as shown in Figure 11. This large amplitude (~ 20 K), is found only around mountainous islands (i.e., Sumatra and Kalimantan). In contrast, the amplitude of Kelvin waves around the equator (over the western Pacific ocean) is generally ~ 10 K in this model simulations (not shown). It is possible that the amplitude of simulated Kelvin waves in this experiment was greatly influenced by model topography, background wind, and stability. Also, observations of large amplitude, tropopause Kelvin waves indicate an amplitude of ~ 10 K (see Figures 2 and 7 in Randel and Wu [2005] and Figure 2d in Yamamoto et al. [2007]). Again, the NICAM generates much larger amplitude Kelvin waves over the Indonesian maritime continent or near mountains, and thus the amplitude values should be viewed with caution.

[31] Another large-scale eastward-propagating (24 m s^{-1}) low temperature signal is seen at 18.4 km (see the dashed

line in Figure 16b). This signal is also observed at 16.9 km, but is delayed at lower altitudes; the low temperature region is seen from 30 December 2006 to 14 January 2007 at 120°W . Again, the propagating signal around the tropopause can be regarded as Kelvin waves. A cold temperature anomaly remains for ≥ 10 days at a particular longitude at 18.4 km. Its zonal scale is $\sim 20,000$ km. The temperature amplitude around the tropopause increases up to ~ 3 K, even when averaged between 5°S and 5°N . Thus, we conclude that Kelvin waves that generate large-scale, low-temperature regions make a significant contribution to temperature variations around the tropopause.

[32] In Section 5.2, we discussed in detail the TTL temperature variations associated with the diurnal variation of deep convection and tropical cyclones. These variations could contribute to dehydration and transport processes around the TTL, locally and regionally. In contrast, in Section 5.3, equatorial Kelvin waves generated by organized convection globally control the temperature variations with large-scale temperature drops.

6. Summary and Concluding Remarks

[33] We have considered the various roles of deep convection in the TTL using a global, nonhydrostatic atmospheric model, NICAM, calculated on a horizontal grid interval of 7 km, under realistic conditions over the period between 15 December 2006 and 15 January 2007. General characteristics such as the zonal mean fields, average

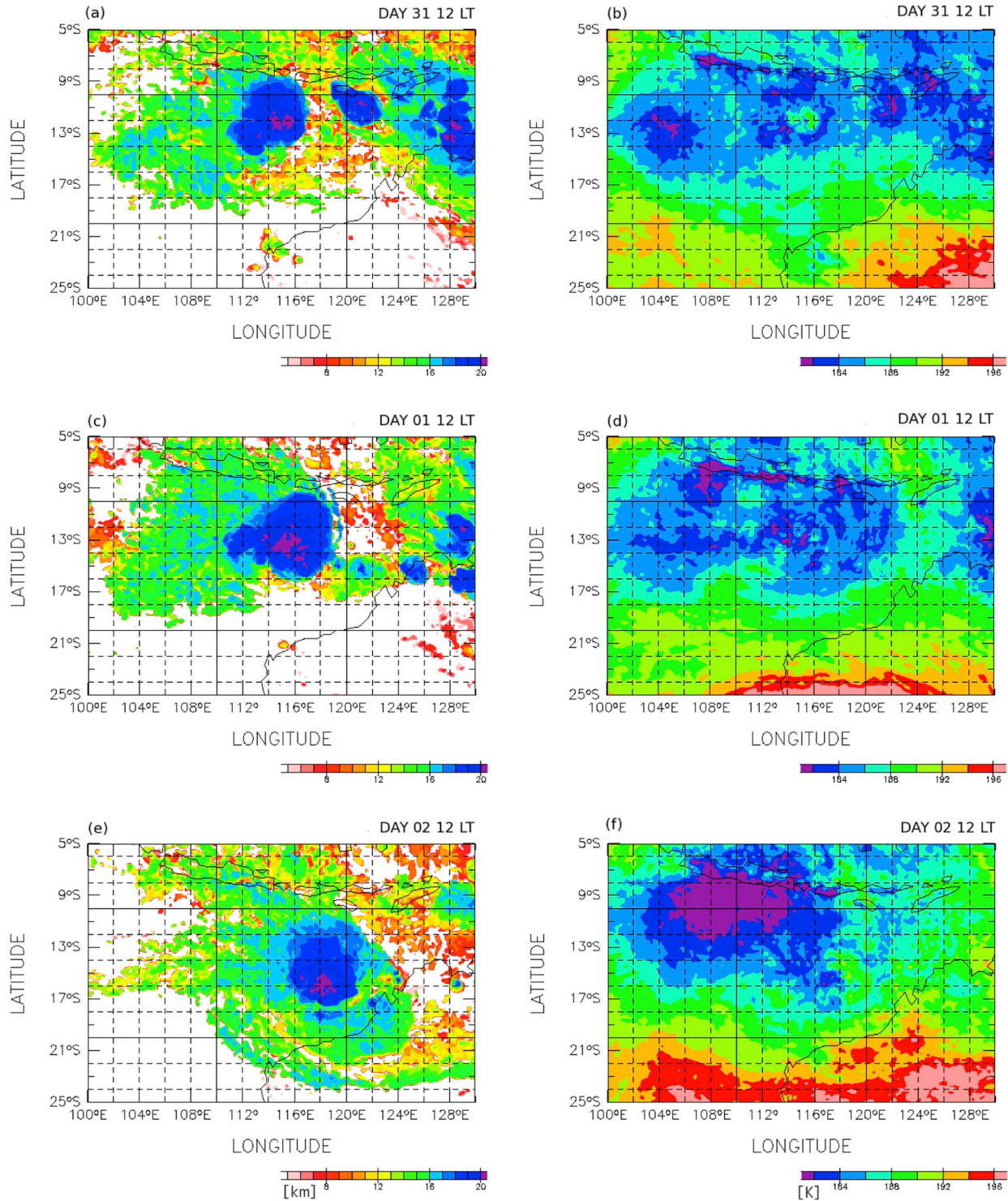


Figure 15. As for Figure 12, but for the tropical cyclone Isobel at 12 LT on 31 December 2006, 1 and 2 January 2007.

profiles, and large-scale convective patterns (including the MJO activity) were found to agree reasonably well with the atmospheric observations. The frequency distribution of vertical winds was compared with that from the EAR data. Both showed that vertical wind speeds are generally confined

to $\pm 3 \text{ m s}^{-1}$, and that the frequency of light winds is lower around 10–15 km than in upper and lower altitude regions. This suggests that the altitude of 10–15 km can be regarded as a mass flux boundary.

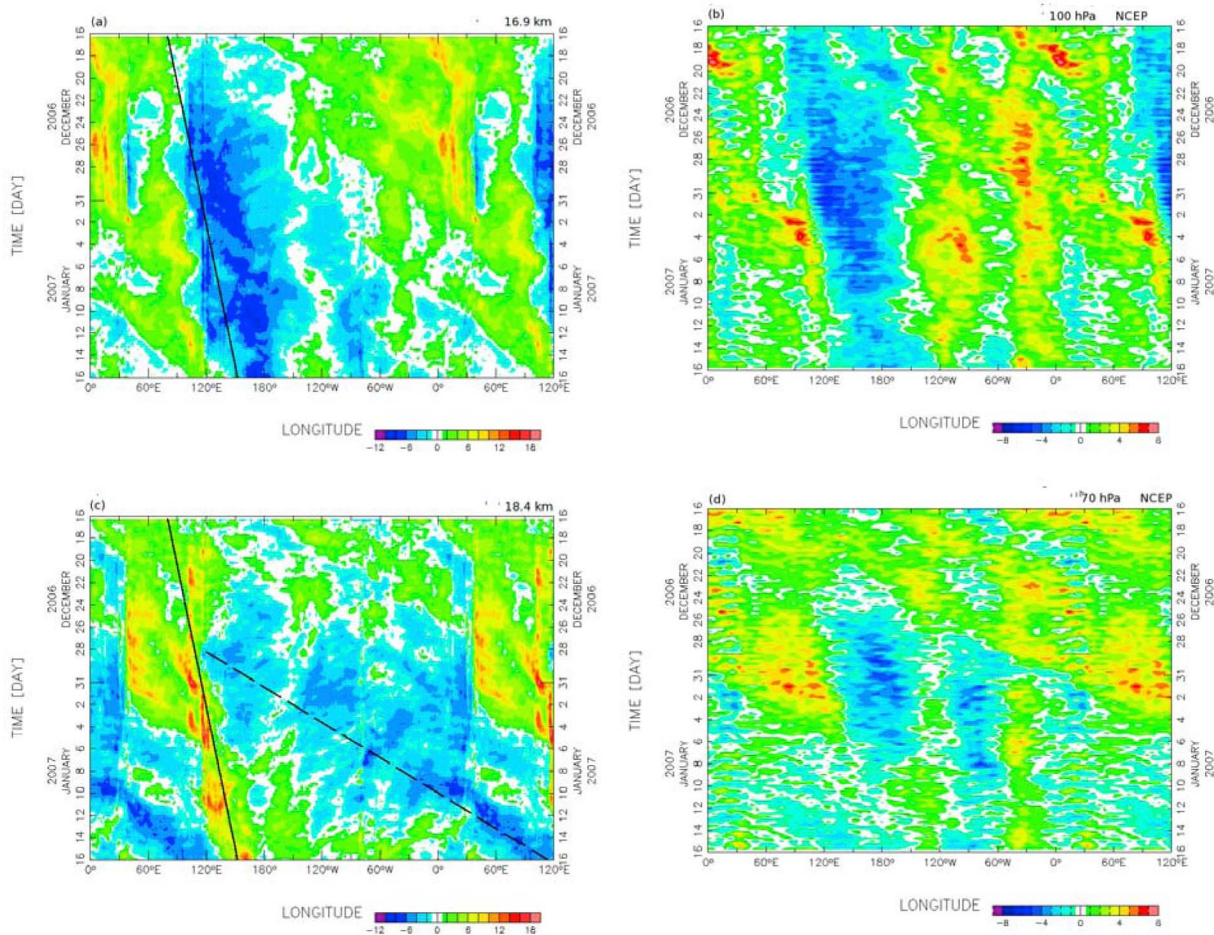


Figure 16. Longitude-time distributions of the temperature anomaly at (a) 16.9 km and (b) 18.4 km, averaged between 5°S and 5°N , using NICAM data, and (c) 100 hPa and (d) 70 hPa, averaged between 5°S and 5°N , using the NCEP1 data. The anomaly is with respect to the average value between 0° and 360° , and for the model integration period (16 December 2006 to 15 January 2007). Note that the region 0° – 120°E is duplicated. The solid slanted line in each panel corresponds to that in Figure 1a. The dashed black line in Figure 16b corresponds to the eastward propagating phase speed of 24 m s^{-1} , starting at 120°E on 28 December 2006. Note that the increment for the color bar of NICAM data is a factor of ~ 2 greater than that for NCEP1 data.

[34] The regional and local-time characteristics of deep convective activity were analyzed. Deep convective activity that directly affects the TTL was found over the southern African continent, Indian Ocean, Indonesia maritime continent through the tropical western Pacific, and the South American continent. We compared the CPC-IR observational data with the NICAM results. The regions of deep convective activity simulated by the NICAM were largely consistent with those in the real atmosphere. Over land, deep convective clouds show clear diurnal variations and are most often observed in the local evening. Over the ocean, deep convective clouds are found over the ITCZ, SPCZ, and in the vicinity of large islands in Indonesia, and are mainly associated with transient disturbances such as tropical cyclones and the MJO. Deep convective activity in the NICAM was prominent over the land. The land-ocean contrast in the deep convective activity is generally consistent

with satellite observations by *Liu and Zipser* [2005] and *Iwasaki et al.* [2010]. However, there is a problem regarding the phase lag, which appears to be caused by the microphysical scheme used in the NICAM. *Masunaga et al.* [2008] showed that the condensation (snow) in the NICAM does not fall rapidly enough and remains for a longer time in the upper troposphere. Therefore, in the present case where the same microphysical scheme is used, the late maximum in convective activity is probably due to the use of this particular microphysical scheme. It should be noted that diurnal variations in clouds penetrating the TTL and the lower stratosphere are first discussed in this paper.

[35] The NICAM simulated multiscale clouds well; i.e., diurnal variations, tropical cyclones (mesoscale), and the MJO (global scale), were all as observed in the real atmosphere. Consequently, we compared the influence of these multiscale clouds on TTL temperature variations.

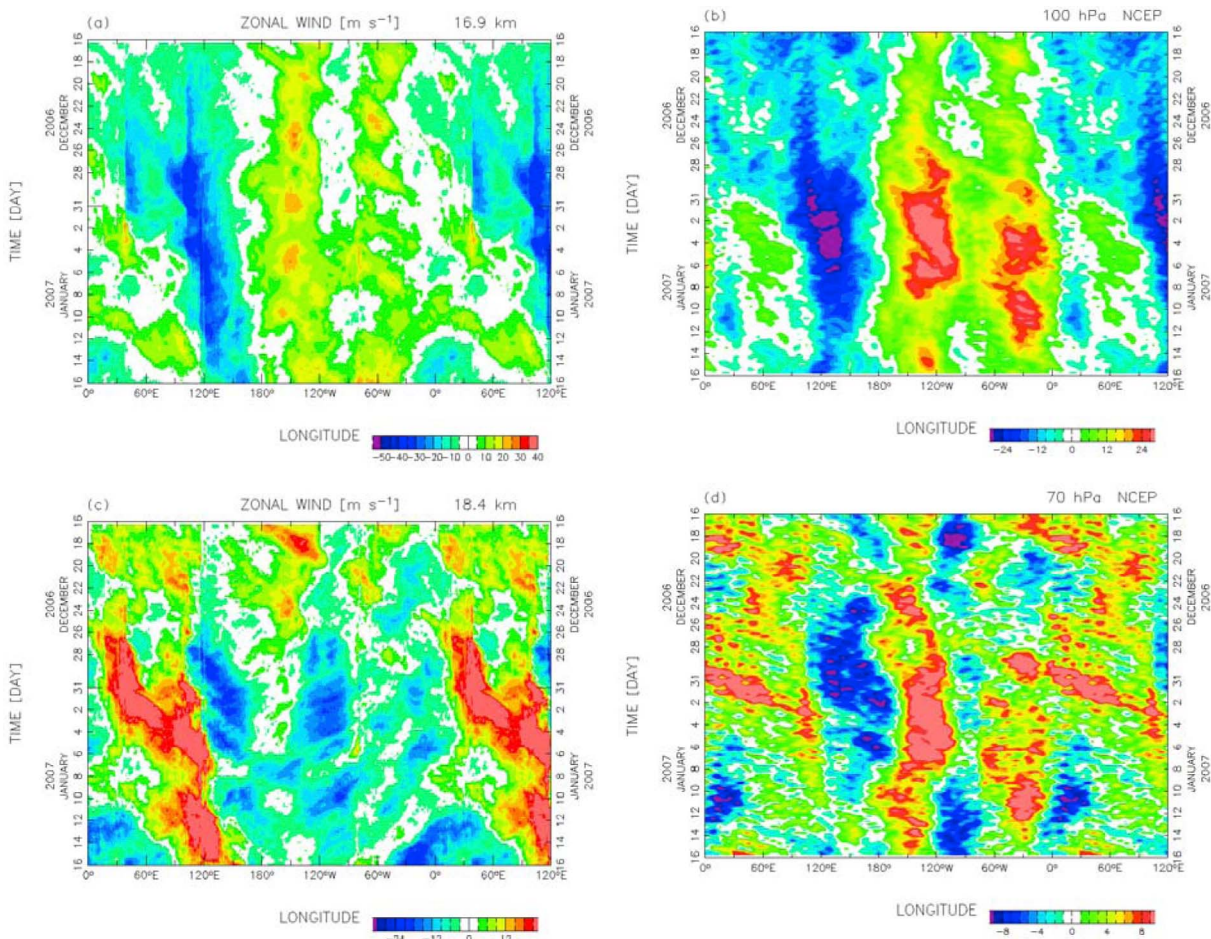


Figure 17. As for Figure 16, but for zonal wind. Note that the increment for the color bar of NICAM data is a factor of ~ 2 greater than that for NCEP1 data.

Temperature variations around the tropopause were investigated in association with (1) local deep convective activity, (2) tropical cyclones, and (3) equatorial Kelvin waves and MJO. Regarding deep convective activity, high variability was found over the east African continent, the Indonesian maritime continent through the western Pacific, the Andes, and Tibet. Diurnal variations of tropopause temperature with an amplitude of ~ 10 K were found over the Indonesian maritime continent. Diurnal cycles of deep convective activity should be the major factor in the diurnal variations. These diurnal variations are superimposed on large, low-frequency temperature variations associated with Kelvin waves, which have an amplitude of ~ 10 K.

[36] We investigated the role of two tropical cyclones, Bond and Isobel, that developed in the real atmosphere. Low temperature regions associated with these tropical cyclones were observed over the convective core and near, but not above, the convection core. Low temperature regions in Bond were caused not only by deep convection, but also by gravity waves generated by the tropical cyclone. The temperature drop associated with deep convection was up to ≥ 6 K, and covered a horizontal extent of ~ 500 km, while the drop associated with gravity waves reached ~ 2 K, with a

horizontal extent of ~ 1000 km. The generation mechanism of the low temperature region associated with Isobel is not clear. These two examples highlight the potential role of tropical cyclone, and related gravity wave generation, in TTL dehydration.

[37] Finally, in a similar manner to the results from the NICAM aqua planet experiments of Kubokawa *et al.* [2010], we found that temperature variations around the tropopause are globally controlled by equatorial Kelvin waves with a zonal phase speed of 3 m s^{-1} in the eastern hemisphere, and 24 m s^{-1} in the western hemisphere. The former were directly generated by the MJO convection with a strong easterly background wind. We conclude that large-scale low temperature regions in the TTL are mainly caused by Kelvin waves generated by large-scale organized convection such as the MJO, even in the real atmosphere affected by islands and continents.

[38] It should be noted that unrealistic large temperature variations are simulated in the NICAM. This is probably due to the relatively coarse vertical resolution. Kelvin waves generated by organized convection control the temperature field in the TTL at a planetary scale. The impact of these waves in the TTL and lower stratosphere continues for more

than two weeks. In association with tropical cyclones, the TTL temperature can change by ~ 6 K at a cyclonic scale (~ 500 km). Gravity waves generated by tropical cyclones also contributed to TTL temperature variations over a region with a horizontal extent of ~ 1000 km in this model simulations. Because tropical cyclones continue to be active for periods of a few days to a week in the tropics, a significant impact on temperature changes may be expected both locally and regionally. Over islands, deep convection with diurnal cycles can also effect the TTL temperature.

[39] **Acknowledgments.** We would like to thank Hirofumi Tomita and other researchers responsible for the development of the NICAM. We thank Fumio Hasebe, Koji Yamazaki, Masato Shiotani, Takeshi Horinouchi, and Tomonori Sato for their invaluable comments. We used the Interpolated OLR data provided by the NOAA/OAR/ESRL PSD, Boulder, Colorado, USA, from their web site at <http://www.esrl.noaa.gov/psd/>. The ERA-Interim data set was obtained from the ECMWF data server. The JRA25 data set was provided from the cooperative research project of the JRA-25 long-term reanalysis by the Japan Meteorological Agency (JMA) and the Central Research Institute of Electric Power Industry (CRIEPI). The NCEP/NCAR Reanalysis data set was provided by the NOAA/OAR/ESRL PSD, Boulder, Colorado, USA, from their web site at <http://www.esrl.noaa.gov/psd/>. Figures 1–16 were produced using the GFD-DENNOU Library. This study was supported in part by the CASIO Science Promotion Foundation, the Circle for the Promotion of Science and Engineering, and the Cooperative Research Program of the Center for Climate System Research, University of Tokyo. The NICAM experiments were performed using the Earth Simulator housed at JAMSTEC.

References

- Alexander, S. P., and T. Tsuda (2008), Observations of the diurnal tide during seven intensive radiosonde campaigns in Australia and Indonesia, *J. Geophys. Res.*, *113*, D04109, doi:10.1029/2007JD008717.
- Barth, M., T. Birner, N. McFarlane, D. Pendlebury, and J. Petch (2007), Modelling of deep convection and chemistry and their roles in the tropical tropopause layer: SPARC-GEWEX/GCSC-IGAC workshop, *SPARC Newsl.*, *28*, 7–11.
- Chaboureaud, J.-P., J.-P. Cammas, J. Duron, P. J. Maseart, N. M. Sitnikov, and H.-J. Voessing (2007), A numerical study of tropical cross-tropopause transport by convective overshoots, *Atmos. Chem. Phys.*, *7*, 1731–1740.
- Danielsen, E. F. (1993), In site evidence of rapid, vertical, irreversible transport of lower tropospheric air into the lower tropical stratosphere by convective cloud turrets and by large-scale upwelling in tropical cyclones, *J. Geophys. Res.*, *98*(D5), 8665–8681.
- Dee, D. P., et al. (2011), The ERA-Interim reanalysis: Configuration and performance of the data assimilation system, *Q. J. R. Meteorol. Soc.*, *137*, 553–597.
- Dessler, A. E., S. P. Palm, and J. D. Spinhirne (2006), Tropical cloud-top height distributions revealed by the Ice, Cloud, and Land Elevation Satellite (ICESat)/Geoscience Laser Altimeter System (GLAS), *J. Geophys. Res.*, *111*, D12215, doi:10.1029/2005JD006705.
- Folkens, I. (2009), A one-dimensional cloud model with trimodal convective outflow, *J. Clim.*, *22*, 6437–6455, doi:10.1175/2009JCLI13134.1
- Folkens, I., M. Loewenstein, J. Podolske, S. J. Oltmans, and M. Proffitt (1999), A barrier to vertical mixing at 14 km in the tropics: Evidence from ozonesondes and aircraft measurements, *J. Geophys. Res.*, *104*(D18), 22,095–22,102.
- Fudeyasu, H., Y. Wang, M. Satoh, T. Nasuno, H. Miura, and W. Yanase (2008), Global cloud-system-resolving model NICAM successfully simulated the lifecycles of two real tropical cyclones, *Geophys. Res. Lett.*, *35*, L22808, doi:10.1029/2008GL036003.
- Fudeyasu, H., Y. Wang, M. Satoh, T. Nasuno, H. Miura, and W. Yanase (2010a), Multiscale interactions in the lifecycle of a tropical cyclone simulated in a global cloud-system-resolving model, Part 1: Large-scale and storm-scale evolutions, *Mon. Weather Rev.*, *138*, 4285–4304, doi:10.1175/2010MWR3474.1.
- Fudeyasu, H., Y. Wang, M. Satoh, T. Nasuno, H. Miura, and W. Yanase (2010b), Multiscale interactions in the lifecycle of a tropical cyclone simulated in a global cloud-system-resolving model, Part 2: Mesoscale and storm-scale processes, *Mon. Weather Rev.*, *138*, 4305–4327, doi:10.1175/2010MWR3475.1.
- Fueglistaler, S., A. E. Dessler, T. J. Dunkerton, I. Folkens, Q. Fu, and P. W. Mote (2009), Tropical tropopause layer, *Rev. Geophys.*, *47*, RG1004, doi:10.1029/2008RG000267.
- Fujiwara, M., and M. Takahashi (2001), Role of the equatorial Kelvin wave in stratosphere-troposphere exchange in a general circulation model, *J. Geophys. Res.*, *106*(D19), 22,763–22,780.
- Fujiwara, M., M. K. Yamamoto, H. Hashiguchi, T. Horinouchi, and S. Fukao (2003), Turbulence at the tropopause due to breaking Kelvin waves observed by the equatorial atmosphere radar, *Geophys. Res. Lett.*, *30*(4), 1171, doi:10.1029/2002GL016278.
- Fujiwara, M., et al. (2009), Cirrus observations in the tropical tropopause layer over the western Pacific, *J. Geophys. Res.*, *114*, D09304, doi:10.1029/2008JD011040.
- Fukao, S., H. Hashiguchi, M. Yamamoto, T. Tsuda, T. Nakamura, M. K. Yamamoto, T. Sato, M. Hagio, and Y. Yabugaki (2003), Equatorial Atmosphere Radar (EAR): System description and first results, *Radio Sci.*, *38*(3), 1053, doi:10.1029/2002RS002767.
- Gettelman, A., and T. Birner (2007), Insights into tropical tropopause layer processes using global models, *J. Geophys. Res.*, *112*, D23104, doi:10.1029/2007JD008945.
- Grosvenor, D. P., T. W. Choulaton, H. Coe, and G. Held (2007), A study of the effect of overshooting deep convection on the water content of the TTL and lower stratosphere from cloud Resolving Model simulations, *Atmos. Chem. Phys.*, *7*, 4977–5002.
- Hendon, H. H., and M. L. Salby (1994), The life cycle of the Madden-Julian oscillation, *J. Atmos. Sci.*, *51*, 2225–2237.
- Highwood, E. J., and B. J. Hoskins (1998), The tropical tropopause, *Q. J. R. Meteorol. Soc.*, *124*, 1579–1604.
- Inoue, T., M. Satoh, H. Miura, and B. Mapes (2008), Characteristics of cloud size of deep convection simulated by a global cloud resolving model, *J. Meteorol. Soc. Jpn.*, *86A*, 17–31.
- Inoue, T., M. Satoh, Y. Hagihara, H. Miura, and J. Schmetz (2010), Comparison of high-level clouds represented in a global cloud system resolving model with CALIPSO/CloudSat and geostationary satellite observations, *J. Geophys. Res.*, *115*, D00H22, doi:10.1029/2009JD012371.
- Iwasaki, S., T. Shibata, J. Nakamoto, H. Okamoto, H. Ishimoto, and H. Kubota (2010), Characteristics of deep convection measured by using the A-train constellation, *J. Geophys. Res.*, *115*, D06207, doi:10.1029/2009JD013000.
- Jain, A. R., S. S. Das, T. K. Mandal, and A. P. Mitra (2006), Observations of extremely low tropopause temperature over the Indian tropical region during monsoon and postmonsoon months: Possible implications, *J. Geophys. Res.*, *111*, D07106, doi:10.1029/2005JD005850.
- Janowiak, J. E., R. J. Joyce, and Y. Yarosh (2001), A real-time global half-hourly pixel-resolution infrared dataset and its applications, *Bull. Am. Meteorol. Soc.*, *82*(3), 205–217.
- Johnson, R. H., T. M. Rickenbach, S. A. Rutledge, P. E. Ciesielski, and W. H. Schubert (1999), Trimodal characteristics of tropical convection, *J. Clim.*, *12*, 2397–2418.
- Kalnay, E., et al. (1996), The NCEP/NCAR 40-year reanalysis project, *Bull. Am. Meteorol. Soc.*, *77*(3), 437–471.
- Kley, D., P. J. Crutzen, H. G. J. Smit, H. Vömel, S. J. Oltmans, H. Grassl, and V. Ramanathan (1996), Observations of near-zero ozone concentrations over the convective Pacific: Effects on air chemistry, *Science*, *274*, 230–233.
- Knutson, T. R., and K. M. Weickmann (1987), 30–60-day atmospheric oscillations: Composite life cycles of convection and circulation anomalies, *Mon. Weather Rev.*, *115*, 1407–1436.
- Kuang, Z., and C. S. Bretherton (2004), Convective influence on the heat balance of the tropical tropopause layer: A cloud-resolving model study, *J. Atmos. Sci.*, *61*, 2919–2927.
- Kubokawa, H., M. Fujiwara, T. Nasuno, and M. Satoh (2010), Analysis of the tropical tropopause layer using the Nonhydrostatic Icosahedral Atmospheric Model (NICAM): Aqua-planet experiments, *J. Geophys. Res.*, *115*, D08102, doi:10.1029/2009JD012686.
- Küpper, C., J. Thuburn, G. C. Craig, and T. Birner (2004), Mass and water transport into the tropical stratosphere: A cloud-resolving simulation, *J. Geophys. Res.*, *109*, D10111, doi:10.1029/2004JD004541.
- Liebmann, B., and C. A. Smith (1996), Description of a complete (interpolated) outgoing longwave radiation dataset, *Bull. Am. Meteorol. Soc.*, *77*, 1275–1277.
- Liu, C., and E. J. Zipser (2005), Global distribution of convection penetrating the tropical tropopause, *J. Geophys. Res.*, *110*, D23104, doi:10.1029/2005JD006063.
- Liu, P., et al. (2009), An MJO simulated by the NICAM at 14-km and 7-km resolutions, *Mon. Weather Rev.*, *137*, 3254–3268, doi:10.1175/2009MWR2965.1.
- Madden, R. A., and P. R. Julian (1972), Description of global-scale circulation cells in the tropics with a 40–50 day period, *J. Atmos. Sci.*, *29*, 1109–1123.
- Madden, R. A., and P. R. Julian (1994), Observations of the 40–50-day tropical oscillation—A review, *Mon. Weather Rev.*, *122*, 814–837.

- Mapes, B. E. (2001), Water's two height scales: The moist adiabat and the radiative troposphere, *Q. J. R. Meteorol. Soc.*, *127*, 2353–2366.
- Masanaga, H., M. Satoh, and H. Miura (2008), A joint satellite and global cloud-resolving model analysis of a Madden-Julian oscillation event: Model diagnosis, *J. Geophys. Res.*, *113*, D17210, doi:10.1029/2008JD009986.
- Mega, T., M. K. Yamamoto, H. Luce, Y. Tabata, H. Hashiguchi, M. Yamamoto, M. D. Yamanaka, and S. Fukao (2010), Turbulence generation by Kelvin-Helmholtz instability in the tropical tropopause layer observed with a 47 MHz range imaging radar, *J. Geophys. Res.*, *115*, D18115, doi:10.1029/2010JD013864.
- Miura, H., M. Satoh, T. Nasuno, A. T. Noda, and K. Oouchi (2007), A Madden-Julian oscillation event realistically simulated by a global cloud-resolving model, *Science*, *318*, 1763–1765.
- Mote, P. W., H. L. Clark, T. J. Dunkerton, R. S. Harwood, and H. C. Pumphrey, (2000), Intraseasonal variations of water vapor in the tropical upper troposphere and tropopause region, *J. Geophys. Res.*, *105*(D13), 17,457–17,470.
- Nasuno, T., H. Miura, M. Satoh, A. T. Noda, and K. Oouchi (2009), Multi-scale organization of convection in a global numerical simulation of the December 2006 MJO event using explicit moist process, *J. Meteorol. Soc. Jpn.*, *87*, 335–345, doi:10.2151/jmsj.87.335.
- Nishi, N. (1989), Observational study on the 30–60 day variations in the geopotential and temperature fields in the equatorial region, *J. Meteorol. Soc. Jpn.*, *67*(2), 187–203.
- Onogi, K., et al. (2007), The JRA-25 Reanalysis, *J. Meteorol. Soc. Jpn.*, *85*, 369–432.
- Potter, B. E., and J. R. Holton (1995), The role of monsoon convection in the dehydration of the lower tropical stratosphere, *J. Atmos. Sci.*, *52*(8), 1034–1050.
- Randel, W. J., and F. Wu (2005), Kelvin wave variability near the equatorial tropopause observed in GPS radio occultation measurements, *J. Geophys. Res.*, *110*, D03102, doi:10.1029/2004JD005006.
- Ratnam, M. V., T. Tsuda, M. Shiotani, and M. Fujiwara (2005), New characteristics of the tropical tropopause revealed by CHAMP/GPS measurements, *SOLA*, *1*, 185–188, doi:10.2151/sola.2005-048.
- Sato, T., H. Miura, M. Satoh, Y. N. Takayabu, and Y. Wang (2009), Diurnal cycle of precipitation in the tropics simulated in a global cloud-resolving model, *J. Clim.*, *22*, 4809–4826, doi:10.1175/2009JCLI2890.1
- Satoh, M., T. Matsuno, H. Tomita, H. Miura, T. Nasuno, and S. Iga (2008), Nonhydrostatic Icosahedral Atmospheric Model (NICAM) for global cloud resolving simulations, *J. Comput. Phys.*, *227*, 3486–3514.
- Satoh, M., T. Inoue, and H. Miura (2010), Evaluations of cloud properties of global and local cloud system resolving models using CALIPSO and CloudSat simulators, *J. Geophys. Res.*, *115*, D00H14, doi:10.1029/2009JD012247.
- Seidel, D. J., R. J. Ross, and J. K. Angell (2001), Climatological characteristics of the tropical tropopause as revealed by radiosondes, *J. Geophys. Res.*, *106*(D8), 7857–7878.
- Seidel, D. J., M. Free, and J. Wang (2005), Diurnal cycle of upper-air temperature estimated from radiosondes, *J. Geophys. Res.*, *110*, D09102, doi:10.1029/2004JD005526.
- Sherwood, S. C., J.-H. Chae, P. Minnis, and M. McGill (2004), Underestimation of deep convective cloud tops by thermal imagery, *Geophys. Res. Lett.*, *31*, L11102, doi:10.1029/2004GL019699.
- Suzuki, J., and M. Shiotani (2008), Space-time variability of equatorial Kelvin waves and intraseasonal oscillations around the tropical tropopause, *J. Geophys. Res.*, *113*, D16110, doi:10.1029/2007JD009456.
- Suzuki, J., M. Shiotani, and N. Nishi (2010), Lifetime and longitudinal variability of equatorial Kelvin waves around the tropical tropopause region, *J. Geophys. Res.*, *115*, D03103, doi:10.1029/2009JD012261.
- Tomita, H., and M. Satoh (2004), A new dynamical framework of nonhydrostatic global model using the icosahedral grid, *Fluid Dyn. Res.*, *34*, 357–400.
- Tomita, H., H. Miura, S. Iga, T. Nasuno, and M. Satoh (2005), A global cloud-resolving simulation: Preliminary results from an aqua planet experiment, *Geophys. Res. Lett.*, *32*, L08805, doi:10.1029/2005GL022459.
- Vömel, H., and K. Diaz (2010), Ozone sonde cell current measurements and implications for observations of near-zero ozone concentrations in the tropical upper troposphere, *Atmos. Meas. Tech.*, *3*, 495–505.
- World Meteorological Organization (2007), Scientific assessment of ozone depletion: 2006, *Rep. 50*, 572 pp., Global Ozone Res. and Monit. Proj., Geneva, Switzerland.
- Yamamoto, M. K., N. Nishi, T. Horinouchi, M. Niwano, and S. Fulao (2007), Vertical wind observation in the tropical upper troposphere by VHF wind profiler: A case study, *Radio Sci.*, *41*, RS5002, doi:10.1029/2005RS003333.